Article

Atomic-Level Structure of Mesoporous Hexagonal Boron Nitride Determined by High-Resolution Solid-State Multinuclear Magnetic Resonance Spectroscopy and Density Functional Theory Calculations

Rick W. Dorn, Patrick M. Heintz, Ivan Hung, Kuizhi Chen, Jin-Su Oh, Tae-Hoon Kim, Lin Zhou, Zhehong Gan, Wenyu Huang,* and Aaron J. Rossini*

Read Online

ACCESS | Metrics & More | Article Recommendations | Supporting Information

ABSTRACT: Mesoporous hexagonal boron nitride (p-BN) has received significant attention over the last decade as a promising candidate for water cleaning/pollutant removal and hydrogen storage applications. Here, high-resolution solid-state NMR spectroscopy and plane-wave density-functional theory (DFT) calculations are used to obtain an atomic-level description of p-BN. $^1H-^{15}N$ or $^1H-^{14}N$ heteronuclear (HETCOR) correlation experiments recorded with either conventional NMR at room temperature or dynamic nuclear polarization surface-enhanced spectroscopy (DNP-SENS) at *ca.* 100 K reveal NB_2H, NBH_2, NBH_3^+ species residing on the edges of BN sheets. Ultra-high field 35.2 T ^{11}B NMR spectroscopy was used to resolve ^{11}B NMR signals from BN_3, $BN_2O_x(OH)_{1-x}$ ($x = 0-1$), $BNO_x(OH)_{2-x}$ ($x = 0-2$), $BO_x(OH)_{3-x}$ ($x = 0-3$), and $BO_x(OH)_{4-x}^-$ ($x = 0-4$). Importantly, 2D ^{11}B dipolar double-quantum−single-quantum homonuclear correlation spectra reveal that many pore/defect sites are composed of boron oxide/hydroxide clusters connected to the BN framework through BN_2O units. 1D and 2D $^{11}B\{^{15}N\}$ HETCOR NMR experiments, in addition to plane-wave DFT calculations of nine different structural models, further confirm the assignment of all NMR signals. The detailed structure determination of the pore and edge/defect sites within p-BN should further enable the rational design and development of next-generation p-BN-based materials. In addition, the techniques outlined here should be applicable to determine structure within other porous and/or boron-based materials.
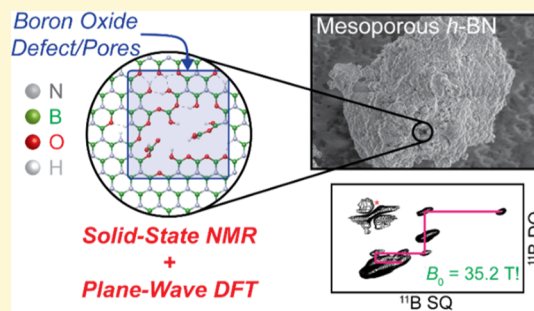
INTRODUCTION

High-surface area, porous materials are of great importance. From metal−organic frameworks to activated carbon and mesoporous silica and zeolites, the ability to tune porosity has provided materials for applications such as water cleaning/pollutant removal,[1−5] gas adsorption,[6−9] separation,[6,10−12] electronics,[9,13−15] and catalysis.[8,10,11,16−20] The introduction of porosity to bulk materials, such as carbon (yielding porous/activated carbon), is commonly used to increase the specific surface area (SSA) and induce various defects or functional groups that can alter the chemical, physical, and electronic properties. Porous hexagonal boron nitride (p-BN), an isoelectronic analogue to activated carbon, has been shown to be a promising candidate for water cleaning,[5,21−33] H_2 storage,[21,23,34−38] and high performance electronics.[39] On its own, hexagonal BN (h-BN; bulk, nanotubular, and 2D nanosheets) has received significant attention in materials science applications due to its high thermal oxidative resistance (>800 °C),[40−43] catalytic activity,[44−48] high bandgap,[49−52] optical properties,[53−56] and low cost.

Similar to activated carbon, the first syntheses of p-BN utilized templating reagents, such as activated/mesoporous carbon,[57−59] silica,[59−61] and zeolites,[62] that provided an existing porous framework that may be completely removed after BN substitution. Template-assisted p-BN syntheses typically result in materials with SSAs of *ca.* 175−600 m² g⁻¹, significantly lower than that of activated/mesoporous carbon analogues prepared *via* similar methods (*ca.* 780−1260 m² g⁻¹).[57,58] In 2013, multiple groups developed template-free syntheses to produce p-BN materials with high SSAs on the order of 960−2078 m² g⁻¹.[5,22,23,34,36] Since then, further work has been devoted to the template-free synthesis of p-BN .[25,30,33,37,63−68] The molecular functionality of the pore and defect sites within p-BN likely gives rise to its superb adsorption properties. Therefore, a detailed
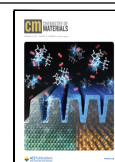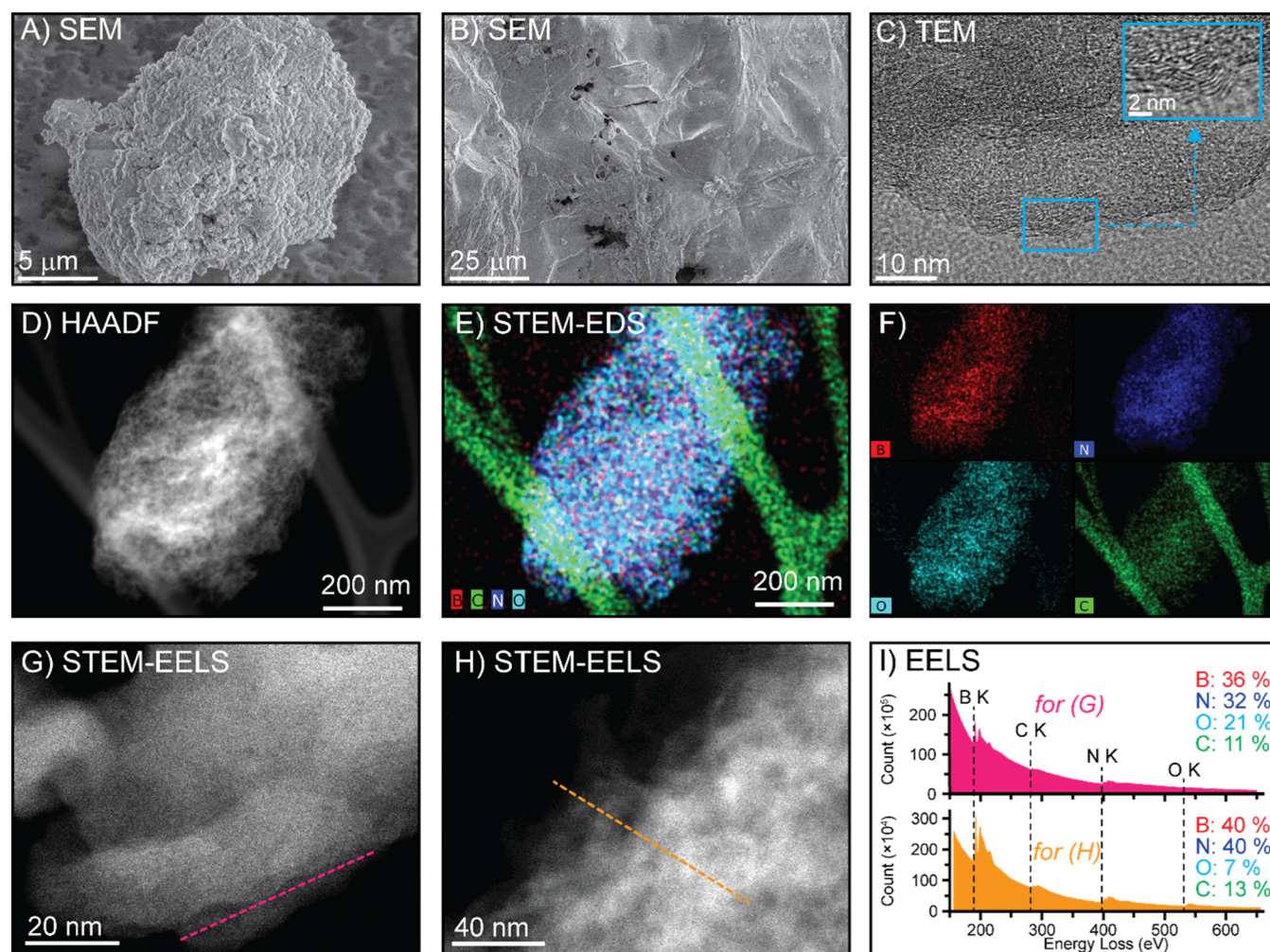
Figure 1. (A,B) SEM, (C) TEM, and (D) high-angle annular dark-field (HAADF) scanning TEM (STEM) images of p-BN. (E,F) Color composite scanning TEM (STEM) energy-dispersive X-ray spectroscopy (STEM−EDS) images of p-BN. Boron, nitrogen, oxygen, and carbon are represented in red, blue, cyan, and green, respectively. (G,H) STEM electron-energy loss spectroscopy (STEM−EELS) images of p-BN. (I) EELS spectra for the dashed lines, as shown in (G,H). The color of the spectrum corresponds to the color of the line in (G,H), that is, (upper) pink corresponds to (G) and (lower) orange corresponds to (H), respectively. Percentages correspond to the average elemental composition over the dashed line.

understanding of the atomic-level structure of pores and defect sites is highly desirable to facilitate the establishment of a structure−function relationship and enable the rational design and development of next-generation adsorption materials. However, common characterization techniques, such as electron microscopy, powder X-ray diffraction, Fourier transform infrared (FTIR), Raman and X-ray photoelectron spectroscopies, often provide an incomplete picture of the molecular structure.[5,34,65,68]

High-resolution magic angle spinning (MAS) solid-state NMR spectroscopy is a powerful technique to probe atomic-level structure within crystalline and amorphous solids. Takegoshi and co-workers have applied high-field (21.8 T) ^{11}B solid-state NMR spectroscopy to study the structure of p-BN and mesoporous boron carbon nitride (p-BCN) produced by template synthesis.[69] In addition to ^{11}B NMR signals associated with h-BN, they observed several additional ^{11}B NMR peaks in p-BN assigned to carbon-doped h-BN (BCN) and cubic boron nitride (c-BN). Schlienger *et al.* utilized 1D ^{11}B solid-state NMR spectroscopy to show that p-BN templated from zeolites contains both major BN_3 and minor BO_3 species.[62] Typically, defect/pore sites within a bulk material are terminated by

hydrogen-containing functional groups, whereas the bulk framework is hydrogen free. Therefore, defect/pore sites can be selectively probed by transferring nuclear polarization from ^{1}H to the nucleus of interest.[70−74] For example, we recently used a combination of [1]H−[11]B, [1]H−[14]N, and [1]H−^{15}N solid-state NMR spectroscopy experiments to selectively show that the edges of 2D h-BN nanosheets are terminated with boron oxide/hydroxide and amine functional groups.[75] Dipolar-based hetero- and homonuclear correlation NMR experiments can be further used to probe the spatial connectivity between nuclear spins, allowing for the complete determination of the molecular structure. Recently, we demonstrated the powerful use of ultra-high field 35.2 T [11]B dipolar double-quantum−single-quantum (DQ−SQ) solid-state NMR spectroscopy to probe the molecular structure within boron-based oxidative dehydrogenation heterogenous catalysts.[76]

In this contribution, we use high-resolution ^{1}H, [11]B, ^{14}N, and ^{15}N solid-state NMR spectroscopy, in conjunction with periodic plane-wave density-functional theory (DFT) calculations, to probe the atomic-level structure within p-BN. The p-BN material studied here was synthesized by the high temperature (1050 °C) decomposition of boric acid, melamine, and urea,

following previously reported template-free protocols.[65,68] Electron microscopy images of p-BN illustrates a highly porous and defective material, consistent with a high surface area material. ^{1}H−^{15}N heteronuclear correlation experiments performed on ^{15}N-enriched p-BN at either room temperature or low temperature (∼100 K) identify distinct nitrogen environments assigned to NB_3, NB_2H, NBH_2, NBH_3^+, and NH_4^+. The identification of NB_3, NB_2H, and NBH_3^+ was further confirmed by recording a fast MAS ^{1}H{^{14}N} HMQC spectrum of p-BN. Ultra-high field 35.2 T ^{11}B solid-state NMR experiments were used to reduce quadrupolar broadening for probing all boron species within p-BN. Most importantly, 35.2 T ^{11}B dipolar DQ−SQ homonuclear correlation spectra of p-BN reveal the spatial connectivity of all boron species, suggesting that many of the pores and defect sites within p-BN are composed of boron oxide/hydroxide clusters connected to the BN framework. 2D ^{11}B−^{15}N HETCOR spectra of ^{15}N-enriched p-BN recorded with or without ^{1}H → ^{11}B cross-polarization (CP) at the start of the experiment suggest that most of the BN framework is terminated by boron hydroxide or boron oxide; however, amine edge terminations are also present. Lastly, plane-wave DFT calculations were used to build structural models and confirm the assignment of all ^{11}B, ^{14}N, and ^{15}N NMR signals. The detailed structural characterization presented here provides an atomic-level description of the molecular structure composing pore and defect sites within p-BN.

■ RESULTS AND DISCUSSION

General Characterization of p-BN. Scanning electron microscopy (SEM) is commonly used to gain insights into the three-dimensional morphology of a material. SEM images of p-BN reveal that the particle sizes are on the order of micrometers and that the morphology is extensively disordered with many large pores (Figures 1A,B and S1A), typical of high SSA materials.[68] The extent of disorder through random stacking of BN sheets can more clearly be seen through transmission electron microscopy (TEM) images of p-BN (Figures 1C and S1B−I). Closer examination of the TEM images reveals the presence of stacked BN sheets that are not perfectly flat, as would be observed in bulk h-BN or 2D h-BN nanosheets (Figures 1C, S1C and S1I). Rather, the BN exhibits minimal long range-order, consistent with a highly porous and defective material.

STEM coupled with energy-dispersive X-ray spectroscopy (STEM−EDS) was used to probe the elemental distribution within a p-BN particle (Figure 1D−F). STEM−EDS images reveal that B, N, O, and C atoms are homogenously distributed throughout the particle (Figure 1E,F). Electron-energy loss spectroscopy (EELS) is generally a more quantitative technique to determine elemental composition with lighter atoms. EELS spectra composed from two regions within a p-BN particle again reveal the presence of B, N, O and C atoms (Figure 1G−I). The ratio of B/N is close to the expected 1:1 ratio for BN, while the B, N, C, and O elemental compositions vary either due to sample thickness variation, carbon grid effect, or local structural differences in the material (Figure 1I). Nevertheless, STEM−EDS and STEM−EELS reveal the presence of O and C atoms (dopants) within the p-BN particles. A powder X-ray diffraction spectrum of p-BN reveals two broad peaks at 2θ values of ca. 26 and 42° that correspond to the (002) and (100) diffraction planes, respectively (Figure S2).[65,68] The broad diffraction peaks confirm that p-BN is highly disordered and non-crystalline, in agreement with the electron microscopy images discussed

above. A FTIR spectrum of p-BN shows a broad, intense feature at ca. 1355 cm^{-1} corresponding to B−N stretching (Figure S3). Importantly, there is a broad feature centered around ca. 3200 cm^{-1}, suggesting the presence of many hydroxyl and/or amine functional groups (Figure S3). Below, solid-state NMR spectroscopy and DFT calculations are used to more precisely determine atomic-level structure within p-BN.

^{15}N and ^{14}N Solid-State NMR Spectroscopy. Nitrogen has two NMR-active isotopes, ^{14}N and ^{15}N, where ^{15}N is typically the preferred nucleus for NMR spectroscopy because it is a spin I = 1/2 nucleus, whereas ^{14}N is a spin I = 1 quadrupolar nucleus which gives rise to broad NMR spectra. However, the low natural isotopic abundance of ^{15}N (0.37%) typically requires ^{15}N labeling or the use of sensitivity-enhanced NMR spectroscopy techniques, such as dynamic nuclear polarization (DNP). Here, ^{1}H−^{15}N heteronuclear correlation (HETCOR) NMR experiments were performed on a ^{15}N-enriched p-BN material. ^{15}N-enrichment of p-BN and other nitride materials is often straightforward because inexpensive 99% ^{15}N-labeled urea (ca. $100 per 0.25 g) can be incorporated into the synthesis.[77] It should be noted that the ^{15}N isotopic abundance in p-BN is likely less than 50% because melamine, one of the other precursors, contains natural isotopic abundance nitrogen that likely also incorporates into the p-BN structure.

A 2D ^{1}H → ^{15}N CP HETCOR NMR spectrum of ^{15}N-enriched p-BN was recorded at B_0 = 9.4 T with 25 kHz MAS, a 5 ms CP contact time, and 100 kHz ^{1}H radio frequency (RF) field of eDUMBO$_{1−22}$ homonuclear dipolar decoupling during the indirect acquisition of ^{1}H (Figure 2A).[78] A ^{1}H{^{15}N} CP-HETCOR spectrum obtained with 50 kHz MAS and ^{1}H detection also shows the same sets of ^{1}H and ^{15}N NMR signals (Figure S4A). The 2D CP-HETCOR spectrum reveals four relatively resolved ^{1}H NMR signals at ca. 2, 4.5, 7, and 9 ppm correlating to five unique ^{15}N signals at isotropic shifts of −275 to −290 ppm (purple highlight), −295 to −310 ppm (red highlight), −320 to −335 ppm (blue highlight), −340 to −345 ppm (orange highlight), and −350 to −360 ppm (green highlight). Based on previous literature and our prior analysis of the edge termination of h-BN nanosheets, the ^{15}N NMR signals at ca. −275 to −290 ppm are assigned to NB_3 units, while the ^{15}N NMR signals between −295 and −310 ppm are assigned to NB_2H species.[75,79,80] Closer examination of the ^{15}N NMR signals in the range of −295 to −310 ppm shows that there are two distinct peaks, which corresponds to NB_2H groups residing on armchair (ca. −297 ppm) or zigzag (ca. −305 ppm) edges.[75] The direct excitation ^{15}N spin echo NMR spectrum obtained with a 400 s recycle delay confirms that NB_3 units within the h-BN domains are the predominant nitrogen environment (Figures 2A and 3A, Table S1). The ^{15}N spin echo NMR spectrum may not be fully quantitative due to long ^{15}N longitudinal relaxation time constants (T_1). However, quantitative ^{11}B solid-state NMR spectra suggest that ca. 55% of the p-BN is made up of h-BN domains (vide infra).

1D ^{1}H → ^{15}N CPMAS spectra of ^{15}N-enriched p-BN were recorded with conventional NMR at room temperature (∼300 K) or DNP surface-enhanced spectroscopy (DNP-SENS)[81,82] at ∼100 K (Figure 3A,B). The ^{1}H → ^{15}N CP DNP enhancements (ε) were estimated to be between 3 and 4 (Figure S5). While DNP enhancements were low, the primary benefit of the DNP experiments was the low sample temperature of 100 K which slows molecular motions that partially average ^{15}N heteronuclear dipolar couplings to ^{1}H and ^{11}B. Comparison of the
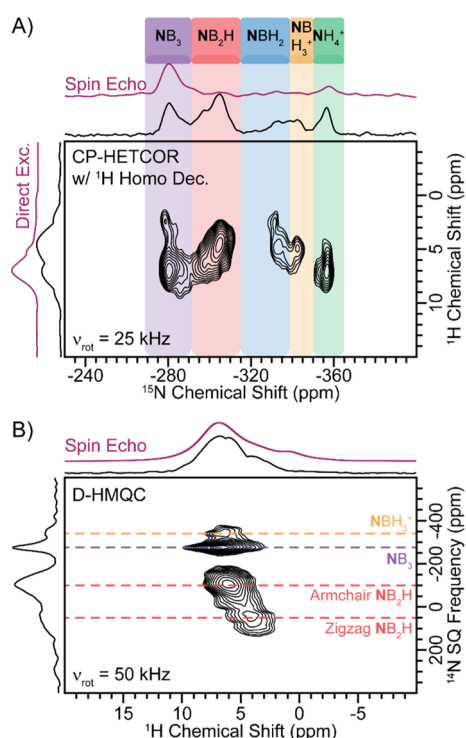
Figure 2. (A) 2D $^1H \rightarrow {}^{15}N$ CP-HETCOR spectrum of ^{15}N-enriched p-BN recorded with ^1H eDUMBO$_{1-22}$ homonuclear dipolar decoupling during ^1H evolution,[78] a 5 ms CP contact time and 25 kHz MAS. (B) 2D $^1H\{^{14}N\}$ dipolar-heteronuclear multiple quantum coherence (D-HMQC) spectrum of p-BN (natural isotopic abundance) recorded with 400 μs of total SR4$_1^2$ heteronuclear dipolar recoupling applied to the ^1H spins and 50 kHz MAS. All spectra were recorded at room temperature with B_0 = 9.4 T.

room temperature $^1H \rightarrow {}^{15}N$ CPMAS spectra recorded with CP contact times of 0.5, 2.0, and 5.0 ms initially suggests that only the ^{15}N resonances between -295 and -345 ppm contain directly attached hydrogen atoms as they were the primary ^{15}N NMR signals observed with a short CP contact time (0.5 ms). A short CP contact time will selectively probe nitrogen species with a short H−N internuclear distance as the rate of signal build-up is dependent on the magnitude of the dipolar coupling constant between the two spins (D_{ij}). Note that D_{ij} is inversely proportional to the cube of the internuclear distance ($D_{ij} \propto r_{ij}^{-3}$). However, at low temperature ($\sim$100 K), the ^{15}N NMR signal at ca. -355 ppm was also observed in the CPMAS spectrum recorded with a CP contact time of 0.1 ms (Figure 3B). Therefore, comparison of the room and low temperature CPMAS spectra suggest that nitrogen species resonating at -355 ppm contains an N−H covalent bond but exhibits significant dynamics at room temperature which average the $^{15}N-^1H$ heteronuclear dipolar couplings. It is important to note that the NB$_3$ ^{15}N NMR signals resonating between -275 and -290 ppm were not observed in the low temperature CPMAS spectrum recorded with a short CP contact time (0.1 ms), further corroborating the assignment of these signals to NB$_3$.

Next, $^{15}N-^1H$ symmetry-based recoupling separated local field (SLF) curves were recorded at room temperature to measure D_{ij} and H−N internuclear distance for each ^{15}N NMR signal (Figure 3C and S6-9).[83−85] In a $^{15}N-^1H$ SLF NMR experiment, $^1H-^{15}N$ heteronuclear dipolar interactions are recoupled, resulting in dephasing of ^{15}N NMR signals of protonated nitrogen atoms. $^1H-^{15}N$ internuclear dipolar

coupling constants and internuclear distances can be determined by comparing the experimental dephasing curve to that of numerical simulations. Following this procedure, H−N internuclear distances for the ^{15}N NMR signals at ca. -305, -333, or -340 ppm were determined to be ca. 1.06, 1.22, or 1.55 Å, respectively (Figures 3C, S7−S9). The N−H internuclear distance of 1.06 Å determined for the ^{15}N NMR signal at ca. -305 ppm further confirms that this signal corresponds to NB$_2$H groups. The N−H internuclear distance of 1.22 Å determined for the ^{15}N NMR signal at ca. -333 ppm is slightly longer than that of the typical N−H bond length of 1 Å. As discussed below, periodic plane-wave DFT calculations suggest that the ^{15}N NMR signals at ca. -320 to -335 ppm correspond to NBH$_2$ species. Therefore, it is not surprising that the experimentally determined N−H bond length is slightly longer than 1 Å as the N−H$_2$ group may experience 180° hops around the N−B bond that could partially dynamically average the $^1H-^{15}N$ dipolar coupling constant. The N−H internuclear distance of 1.55 Å determined for the ^{15}N NMR signal at ca. -340 ppm is significantly longer than a typical N−H bond length. It is well known that RNH$_3$ groups experience rapid C_3 rotation about the R−N bond axis. This rapid C_3 rotation will significantly average out the $^1H-^{15}N$ dipolar interaction by a modulation factor of $P_2(\cos \theta)$, which is the second-order Legendre polynomial and θ is the R−N−H bond angle (109.5°).[86] Accurate N−H internuclear distances can be back calculated by multiplying the experimentally observed internuclear distance (referred to as the dynamically averaged internuclear distance) by $|P_2(\cos \theta)^{1/3}|$ (see Supporting Information for more discussion).[86] Following this procedure, the N−H internuclear distance was determined to be 1.07 Å, confirming that the ^{15}N NMR signal at ca. -340 ppm corresponds to NBH$_3^+$ species. As discussed below, the assignment of the ^{15}N NMR signal at ca. -340 ppm to NBH$_3^+$ species is further supported by periodic plane-wave DFT calculations and by 2D $^1H\{^{14}N\}$ D-HMQC NMR spectroscopy. The ^{15}N NMR signals in the ranges -275 to -290 and -350 to -360 ppm did not show appreciable dephasing in the SLF experiment recorded at room temperature (Figure S6).

$^1H-^{15}N$ distance measurements were also performed at 100 K with DNP-SENS to reduce dynamical averaging of $^1H-^{15}N$ dipolar interactions. $^{15}N\{^1H\}$ DIPSHIFT[87] curves of p-BN suggest that the ^{15}N NMR signals at ca. -305, -333, -340, and -355 ppm exhibit N−H internuclear distance of ca. 0.98, 1.18, 1.40 and 1.80 Å, respectively (Figure 3D). The N−H internuclear distance of ca. 0.98 Å for the ^{15}N NMR signals at ca. -305 ppm is in good agreement with that measured from the room temperature $^{15}N\{^1H\}$ SLF experiment. The N−H internuclear distances measured for the (-333 ppm) NBH$_2$ and (-340 ppm) NBH$_3^+$ ^{15}N NMR signals at low temperature are shorter than that measured at room temperature, further corroborating their assignments and the hypothesis that there are dynamics at room temperature (NBH$_2$: 180° hops around the N−B bond; NBH$_3^+$: C_3 rotation about the B−N bond). Interestingly, the ^{15}N NMR signal at ca. -355 ppm exhibited dipolar dephasing at low temperature but not at room temperature, consistent with the observation that this ^{15}N NMR signal could be observed in the short contact time CPMAS spectra recorded at 100 K, while this signal was attenuated in the short contact time CPMAS spectra recorded at 300 K. The ^{15}N NMR signal at ca. -355 ppm is in the typical region of ammonium ions (NH$_4^+$), as well as four coordinate N in poly-aminoboranes/borazines.[80,88] Therefore, based upon all
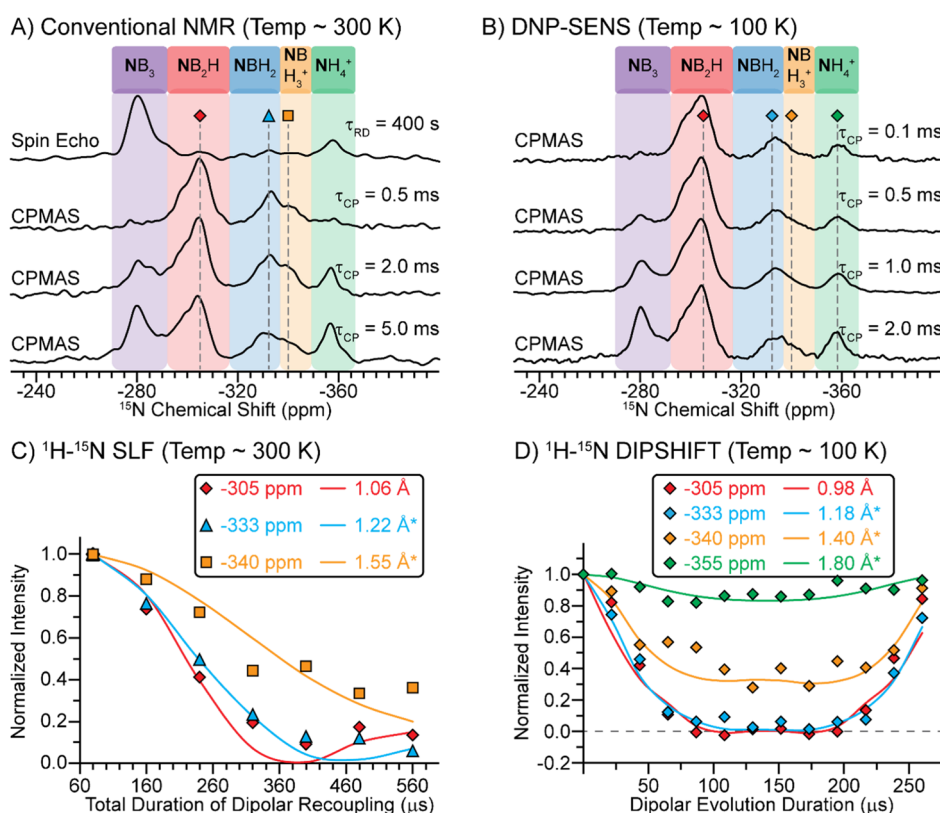
Figure 3. (A,B) Comparison of 1D $^1H \rightarrow {}^{15}N$ CPMAS spectra of ^{15}N-enriched p-BN recorded with (A) conventional NMR at ~300 K with 25 kHz MAS or (B) DNP-SENS at ~100 K with 10 kHz MAS. (A) Direct excitation ^{15}N spin echo NMR spectrum is shown above the CPMAS NMR spectra. (C) $^{15}N\{^1H\}$ symmetry-based recoupling separated local field (SLF) curves recorded with conventional NMR at ~300 K with 25 kHz MAS for the ^{15}N NMR signals at (red diamond) −305 ppm, (blue triangle) −333 ppm, and (orange square) −340 ppm. (D) $^{15}N\{^1H\}$ DIPSHIFT curves recorded with DNP-SENS at ~100 K with 3.846 kHz MAS for the ^{15}N NMR signals at (red diamond) −305 ppm, (blue diamond) −333 ppm, (orange diamond) −340 ppm, and (green diamond) −355 ppm. $^1H \rightarrow {}^{15}N$ CP was implemented at the start of the $^{15}N\{^1H\}$ SLF and DIPSHIFT experiments to enhance overall sensitivity. The best fit SIMPSON numerically simulated SLF or DIPSHIFT curve for each ^{15}N NMR signal is shown by the solid line (Figures S7−S9). SIMPSON numerical simulations were performed with two spins ($^{15}N−^1H_1$), three spins ($^{15}N−^1H_2$), or four-spins ($^{15}N−^1H_3$) to resemble an NB_2H (−305 ppm), NBH_2 (−333 ppm), or NBH_3^+ (−340 ppm) group, respectively (see the Experimental Section for more discussion). Distances marked by an asterisk (*) correspond to N−H species with reduced $^1H−^{15}N$ dipolar coupling constants due to rotational dynamics that partially averages the dipolar coupling constant, yielding a longer apparent internuclear distance. All NMR experiments were recorded at B_0 = 9.4 T.

of the NMR experiments, we tentatively assign the ^{15}N NMR signal at *ca.* −355 ppm to NH_4^+ cations trapped in the pores and/or between BN layers (Figure 3A−B). The assignment of the ^{15}N NMR signal at *ca.* −355 ppm to NH_4^+ was further confirmed by observing $^1H−^{15}N$ *J*-dephasing in a DNP $^{15}N\{^1H\}$ heteronuclear spin echo experiment (Figure S10), as well as no observable dephasing in a $^{15}N\{^{11}B\}$ RESPDOR experiment (see discussion below). We note that Takegoshi *et al.* previously reported c-BN impurities in p-BN synthesized utilizing a carbon template at high temperatures (1750 °C).[69] Prior ^{14}N MAS solid-state NMR spectroscopy of c-BN revealed a narrow ^{14}N NMR signal with an isotropic chemical shift of −360 ppm.[89] While the $^1H−^{15}N$ double resonance NMR experiments discussed above suggest the ^{15}N NMR signal at *ca.* −355 ppm contains attached H atoms, we cannot rule out the possibility of small amounts of c-BN impurities.

Lastly, a 2D $^1H\{^{14}N\}$ D-HMQC spectrum of p-BN (with natural isotopic abundance nitrogen) was recorded at B_0 = 9.4 T with 50 kHz MAS and 400 μs of total SR4$_1^2$ heteronuclear dipolar recoupling applied to the ^1H spins (Figure 2B).[90−96] For spin I = 1/2 nuclei, different isotopes of the same atom yield essentially the same peak position which is determined by the isotropic chemical shift (*e.g.,* ^{111}Cd and ^{113}Cd). However, because ^{14}N is a spin I = 1 quadrupolar nucleus, the frequency at which ^{14}N NMR

signals appear is determined by both the isotropic chemical shift (δ_{iso}, which is the same as for ^{15}N) and the quadrupolar induced shift (QIS). The QIS is proportional to the square of the quadrupolar coupling constant (C_Q), which is dependent on the local symmetry surrounding the nucleus. Spherically symmetric environments yield small C_Q and small or negligible QIS, while less symmetric nitrogen environments possess larger C_Q and significantly positive QIS.[91,97] Here, four main ^{14}N NMR signals were observed at center of gravity peak positions of *ca.* 50, −100, −275, and −340 ppm. Based on our prior analysis of 2D h-BN nanosheets, the ^{14}N NMR signals at *ca.* 50 and −100 ppm can be assigned to NB_2H species residing on a zigzag or armchair edge, respectively.[75] The ^{14}N NMR signal at *ca.* −275 ppm can be assigned to NB_3 species. The NB_3 sites experience a negligible QIS because it is known that the ^{14}N C_Q is only *ca.* 0.1 MHz based upon ^{14}N NMR experiments on h-BN.[75,89,98] Thus, the ^{14}N NMR signal will resonate at the same peak position as the ^{15}N chemical shift, confirming the assignment to NB_3. Likewise, the ^{14}N NMR signal *ca.* −340 ppm resonates at the same peak position as the ^{15}N chemical shift previously assigned to NBH_3^+ species. NBH_3^+ species are expected to adopt a distorted tetrahedral geometry at the nitrogen, resulting in a small C_Q and a ^{14}N NMR signal with a negligible QIS. Therefore, the

observation of the ^{14}N NMR signal at the same chemical shift as the ^{15}N NMR signal further confirms the ^{14}N/^{15}N NMR signal at *ca.* −340 ppm corresponds to NBH_3^+ species. It is worth noting that no ^{14}N NMR signal was observed for the NBH_2 group. As discussed below, periodic plane-wave DFT calculations predict that the ^{14}N C_Q for NBH_2 groups is *ca.* 3 MHz. Therefore, considering lower HMQC efficiency associated with a higher ^{14}N C_Q and significantly larger signal breadth at B_0 = 9.4 T, the NBH_2 ^{14}N NMR signal is likely not observed due to low sensitivity (Figure S11).

In summary, ^{1}H−^{15}N and ^{1}H−^{14}N HETCOR NMR experiments reveal five unique nitrogen species corresponding to NB_3, NB_2H, NBH_2, NBH_3^+, and NH_4^+. NB_3 units lie in the bulk of the material and make up the BN framework, while NB_2H, NBH_2 and NBH_3^+ species likely reside on the edges of the BN sheets. NH_4^+ ions are likely trapped in the pores and/or between BN layers. Below, plane-wave DFT calculations and ^{11}B{^{15}N} HMQC solid-state NMR spectra further corroborate the assignment of all nitrogen species. We note that no ^{14}N/^{15}N NMR signals were assigned to N with directly bonded C heteroatoms. As mentioned above, STEM−EDS and STEM−EELS revealed C atoms homogenously distributed through the p-BN particles. However, DFT calculations suggest that substitution of B for C increases the ^{15}N isotropic chemical shift; substitution of C for B in NB_3 to yield NB_2C increases the isotropic chemical shift from −277 ppm to *ca.* −250 ppm (Figures S18, S19, Table S3, and S4). Furthermore, fully substituted NC_2 or NC_3, as found in graphitic carbon nitride, exhibits ^{15}N isotropic chemical shifts of *ca.* −180 and −225 ppm, respectively.[77] Therefore, we infer that either (i) the atomic weight percent of C is very low and/or (ii) C atoms (dopants) within our samples of p-BN do not exhibit N−C bonds.

Ultra-High Field 35.2 T ^{11}B Solid-State NMR Spectroscopy. Next, we turn to ultra-high field 35.2 T ^{11}B solid-state NMR spectroscopy to probe the structure of boron atoms within p-BN. Because ^{11}B is a half-integer I = 3/2 quadrupolar nucleus, the observable central-transition (CT) is broadened and shifted by the second-order quadrupolar interaction (QI). Therefore, in addition to isotropic chemical shift, the appearance of ^{11}B NMR spectra depends on the electric field gradient (EFG) tensor parameters, C_Q, and asymmetry parameter (η), which are sensitive to the symmetry at the ^{11}B nucleus.[99−101] The broadening of CT ^{11}B NMR signals by the second-order QI is inversely proportional to the applied B_0. Consequently, ^{11}B NMR resolution is proportional to the square of B_0, neglecting other inhomogeneous broadening effects. To maximize ^{11}B resolution, NMR experiments were performed on the series-connected hybrid (SCH) NMR magnet at a field of 35.2 T ($\nu_0(^1$H) = 1500 MHz) at the National High Magnetic Field Laboratory (NHMFL) in Tallahassee, FL.[102] The power of ultra-high field NMR spectroscopy for acquisition of solid-state NMR spectra of half-integer quadrupolar nuclei has been demonstrated for a variety of materials.[76,103−111]

Comparison of 1D direct excitation ^{11}B spin echo NMR spectra recorded at magnetic fields of 9.4, 14.1, 19.6, and 35.2 T illustrates the dramatic increase in ^{11}B NMR resolution with increasing magnetic field strength (Figure S12). All ^{11}B NMR signals observed at 35.2 T are near isotropic in nature (Figure 4), allowing for the straightforward identification of all ^{11}B NMR signals, whereas 2D ^{11}B triple-quantum multiple-quantum MAS (3Q-MQMAS) NMR experiments would be required at more conventional magnetic field strengths (Figures S13 and S14). It is well known that the $\delta_{iso}(^{11}$B) decreases as nitrogen atoms in
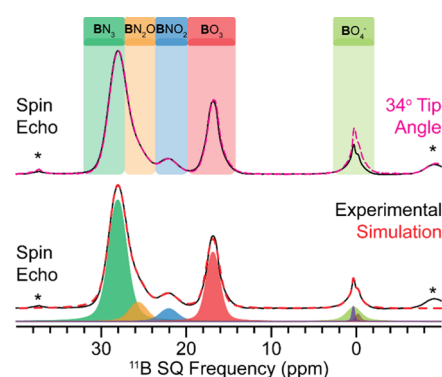

Figure 4. (Upper) 1D ^{11}B direct excitation (black) spin echo and (pink) 34° tip angle single pulse spectra of p-BN recorded at B_0 = 35.2 T with 18 kHz MAS. Colored regions correspond to the degree of BN oxidation (H-atoms are omitted for clarity). (Lower, red-dashed) Analytical simulation of the (black) ^{11}B spin echo spectrum. Asterisks (*) correspond to spinning sidebands.

BN_3 are substituted with oxygen atoms while the C_Q remains relatively constant in the range of 2.5−3.0 MHz.[75,76,101,112,113] Therefore, based on $\delta_{iso}(^{11}$B), the ^{11}B NMR signals can be assigned to BN_3 (δ_{iso} = 28.9 ppm), $BN_2O_x(OH)_{1-x}$ (δ_{iso} = 26.5 ppm, x = 0−1), $BNO_x(OH)_{2-x}$ (δ_{iso} = 22.9 ppm, x = 0−2), $BO_x(OH)_{3-x}$ (δ_{iso} = 17.5 ppm, x = 0−3), and $BO_x(OH)_{4-x}^-$ (δ_{iso} ∼ 0 ppm, x = 0−4) (Figure 4, Table S2). We note that the 3-coordinate ^{11}B species in the experimental ^{11}B NMR spectrum were fit to one site with *ca.* 2 ppm of Gaussian line-broadening to represent a distribution in $\delta_{iso}(^{11}$B), typical of disordered and amorphous materials. Periodic plane-wave DFT calculations and 2D ^{1}H−^{11}B HETCOR, ^{11}B homonuclear dipolar correlation, and ^{11}B{^{15}N} HETCOR NMR spectra confirm the assignment of all ^{11}B NMR signals (*vide infra*). Unless stated otherwise, the oxidized/hydrolyzed boron species will be referred to solely on directly attached heteroatoms, for example, BN_2O could refer to a boron atom with a bridging oxide or hydroxide group coordinated to boron. It should be noted that the $\delta_{iso}(^{11}$B) reported here have a relative error of *ca.* 0.5−1 ppm due to drift of the SCH main magnetic field (see the Experimental Section). However, the field drift does not affect any of the results discussed here.

The relative population of each boron species was determined through analytically simulating the ^{11}B spin echo NMR spectrum recorded at B_0 = 35.2 T (Figure 4, lower and Table S2). Based on the analytical simulation, *ca.* 55% of boron corresponds to BN_3 units, confirming that the majority of p-BN consists of an h-BN framework. Partially oxidized/hydrolyzed BN species, BN_2O and BNO_2, make up *ca.* 8 and 6% of boron atoms, respectively, while fully oxidized/hydrolyzed boron species, BO_3 and BO_4^-, correspond to *ca.* 23 and 8% of boron, respectively. It should be noted that BO_4^- species likely make up slightly more than *ca.* 8% of boron as the overall ^{11}B NMR signal intensity observed in the spin echo experiment was slightly reduced compared to a 34° (π/6) tip angle single-pulse ^{11}B NMR spectrum (Figure 4, upper). We note that Takegoshi *et al.* assigned the 19 ppm and 1 ppm ^{11}B NMR signals to carbon-doped BN and BN_4 in the c-BN phase.[69,114] BN_4 units in c-BN have an $\delta_{iso}(^{11}$B) ∼ 1.5 ppm.[98] We do not rule out the possibility of c-BN impurities (BN_4 units), which would likely overlap with BO_4^- ^{11}B NMR signals. However, based on the ^{15}N NMR spectra and 2D ^{11}B NMR experiments shown below, if c-BN is present, it is in minuscule amounts (<5%). The ^{15}N NMR signal

of c-BN should resonate at −359 ppm, a position similar to the signal observed at −360 ppm, which was assigned to NH_4^+. However, as shown above, the majority of the ^{15}N NMR signals at −360 ppm had attached ^1H spins as evidenced by low temperature CPMAS experiments and $^{15}N\{^1H\}$ J-resolved experiments.

Interestingly, the 1D ^{11}B NMR spectrum illustrates that a significant amount of the p-BN material is made up of oxidized/hydrolyzed boron species. The observation of BO_3 and BO_4^- is consistent with the previously reported ^{11}B solid-state NMR spectra of p-BN that was synthesized utilizing templating reagents.[62,69,114] However, the amount of boron oxide/hydroxide present in the p-BN studied here is significantly higher. Likewise, the surface area of the p-BN material studied here is reported to be significantly higher than that made with templating reagents. As discussed below, the boron oxide/hydroxide species likely compose the pores, defects, and edge sites within p-BN that are connected to the h-BN framework; the BO_3 and BO_4^- ^{11}B NMR signals do not arise from impurities or segregated oxidized phases.

$^1H-^{11}B$ dipolar-based HETCOR experiments were used to probe boron atoms in close spatial proximity to hydrogen atoms. Here, a 2D $^{11}B\{^1H\}$ D-HMQC spectrum of p-BN was recorded at $B_0 = 35.2$ T with 18 kHz MAS and 0.67 ms of total $SR4_1^2$ heteronuclear dipolar recoupling applied to the ^1H spins (Figure 5). An additional 2D $^{11}B\{^1H\}$ D-HMQC spectrum was recorded
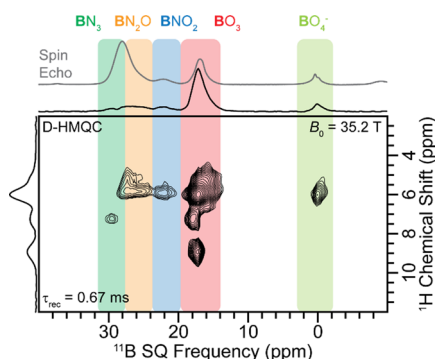

Figure 5. 2D $^{11}B\{^1H\}$ D-HMQC spectrum of p-BN recorded at $B_0 = 35.2$ T with 18 kHz MAS and 0.67 ms of total $SR4_1^2$ heteronuclear dipolar recoupling applied to the ^1H spins. A direct excitation ^{11}B spin echo spectrum (gray) is stacked above the ^{11}B projection of the 2D HETCOR spectrum.

at $B_0 = 19.6$ T (Figure S15). All ^{11}B NMR signals observed in the 1D direct excitation spin echo spectrum reveal correlations to ^1H, suggesting that the pores/defect/edge sites are distributed throughout p-BN. However, the BN_3 signals have attenuated intensity in the 2D $^{11}B\{^1H\}$ D-HMQC spectrum, likely because there are larger BN domains containing BN_3 fragments that are distant from ^1H spins. The BN_3 and oxidized/hydrolyzed BN species (BN_2O and BNO_2) show mainly correlations to a ^1H NMR signal at *ca.* 5.5 ppm. A similar ^1H chemical shift was observed in the 2D $^1H \rightarrow ^{15}N$ CP-HETCOR and $^1H\{^{14}N\}$ D-HMQC spectra. However, it should be noted that both hydroxide and amine ^1H species have a wide chemical shift range in the solid-state, hindering the ability to confirm if they are the same ^1H NMR signals. The fully oxidized/hydrolyzed BO_3 species exhibit correlations to ^1H NMR signals at *ca.* 5.5, 7, and 9 ppm. In addition, the ^{11}B NMR signal for BO_3 is significantly more intense than all other ^{11}B NMR signals. While

the 2D $^{11}B\{^1H\}$ D-HMQC spectra are not quantitative, the near order of magnitude more intense ^{11}B NMR signal suggests that BO_3 contains the highest population of B−OH groups.

Next, we turn to ^{11}B dipolar DQ−SQ homonuclear correlation NMR experiments to probe the spatial connectivity of all boron species within p-BN, further enabling determination of the atomic-level structure.[76,115−121] In a dipolar DQ−SQ NMR experiment, an NMR signal will appear in the indirect DQ dimension at a frequency equal to the sum of the two SQ frequencies of spatially proximate (dipolar coupled) spin pairs.[115] Performing DQ−SQ homonuclear correlation NMR experiments at ultra-high field for half-integer quadrupolar nuclei provides significant line narrowing in both the direct (SQ) and indirect (DQ) dimensions, providing the resolution required to determine the connectivity between all homonuclear spins. The benefits of ultra-high 35.2 T magnetic fields for acquiring dipolar DQ−SQ homonuclear correlation NMR spectra of half-integer quadrupolar nuclei have recently been demonstrated.[76,110]

Here, three 2D ^{11}B dipolar DQ−SQ homonuclear correlation NMR spectra of p-BN were recorded with 0.9, 1.8, or 2.7 ms of total $BR2_2^1$ homonuclear dipolar recoupling and at $B_0 = 35.2$ T with 18 kHz MAS (Figure 6).[115,117] Longer durations of dipolar recoupling will probe further internuclear distances as the build-up of dipolar DQ coherence is dependent on the magnitude of the dipolar coupling constant between the two ^{11}B spins. The ^{11}B DQ−SQ NMR spectrum of p-BN recorded with a short duration of dipolar recoupling (0.9 ms) reveals many auto- and off-diagonal correlations (Figure 6B). Specifically, auto-correlations are observed for all boron species except for BO_4^- (Figure S16). The intense auto-correlations observed for BN_3 confirms the presence of an extended BN framework, while the intense BO_3 auto-correlations suggest that p-BN contains clusters of boron oxide/hydroxide. Intense $BO_3-BO_4^-$ correlations confirm the assignment of the 0 ppm ^{11}B NMR signal to BO_4^- and that the BO_4^- species reside in the boron oxide/hydroxide clusters, likely along the pore edges. Correlations between BN_3-BN_2O, BN_3-BNO_2 and BN_2O-BNO_2 verify that the BN_2O and BNO_2 species are located at the edges of the BN framework. Most importantly, the BO_3-BN_2O correlations reveal that the boron oxide/hydroxide cluster is connected to the BN framework through BN_2O species, where the two nitrogen atoms are connected to the BN framework and the oxygen atom is bridging to the boron oxide/hydroxide cluster. This connection of the boron oxide/hydroxide cluster to the BN framework through BN_2O species is similar to that observed in a catalytically spent oxidative dehydrogenation h-BN catalyst that contains a surface boron oxide/hydroxide phase.[76] Furthermore, the observation that boron oxide/hydroxide is connected to the BN framework is also consistent with 2D ^{11}B SQ−SQ homonuclear correlation experiments performed on mesoporous BCN.[114] However, the aforementioned correlations were previously assigned to a CN-boron domain in close spatial proximity to a BN_3 domain. It should be pointed out that ^{11}B SQ−SQ spin-diffusion homonuclear correlation spectra of p-BN recorded at $B_0 = 19.6$ T also reveal that the boron oxide species are in close spatial proximity to the BN framework (Figure S17). However, the absence of meaningful auto-correlations and lower resolution provided in SQ−SQ spectra recorded with $B_0 = 19.6$ T limited precise identification of the boron connectivity, further illustrating the benefits of the ultra-high field 35.2 T ^{11}B DQ−SQ NMR experiments. As the duration of dipolar recoupling was further
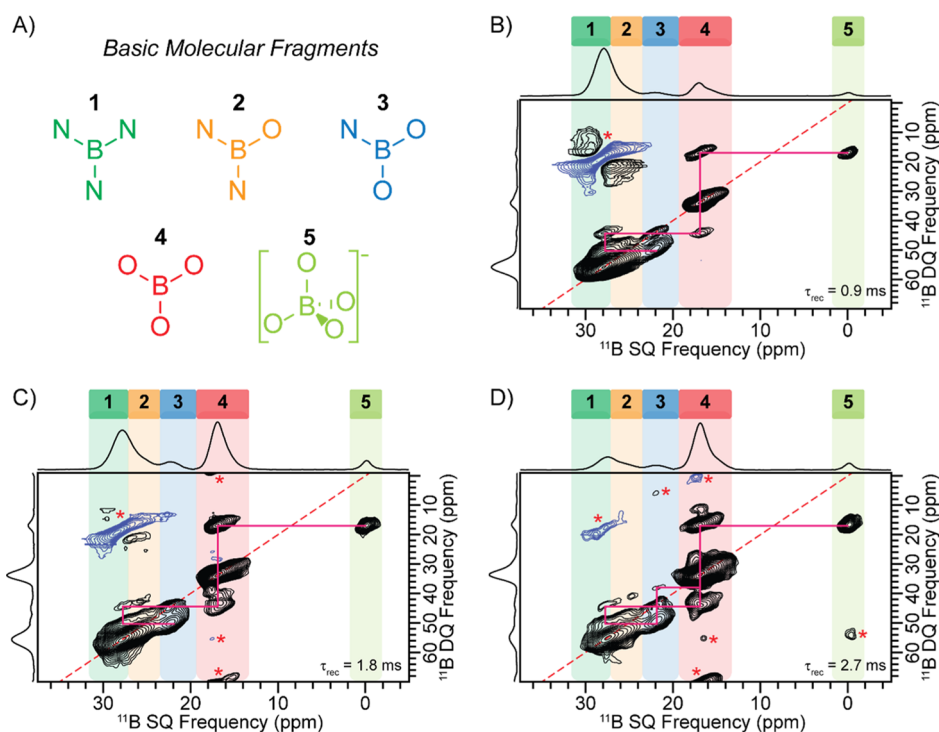
Figure 6. (A) Basic molecular structure of boron fragments in p-BN. (B−D) 2D ^{11}B DQ−SQ spectra of p-BN recorded at B_0 = 35.2 T with 18 kHz MAS and either (B) 0.9, (C) 1.8, or (D) 2.7 ms of total BR2$_2^1$ homonuclear dipolar recoupling. The dashed red lines indicate autocorrelations (DQ frequency = 2 × SQ frequency), and the pink solid lines illustrate the connectivity between correlated ^{11}B species. The red asterisks (*) indicate spinning sidebands.[122]

increased to 1.8 or 2.7 ms, all previously observed homonuclear correlations broaden and round out (Figure 6C,D).

In summary, the correlations observed in the ^{11}B dipolar DQ−SQ NMR spectra illustrate that boron oxide/hydroxide clusters are homogeneously distributed throughout the BN framework, suggesting that these boron oxide/hydroxide clusters likely compose many of the pores and defect sites present within p-BN. Based on the analytical simulation of the 1D 35.2 T ^{11}B spin echo, the **BO$_3$** and **BO$_4^-$** containing boron oxide/hydroxide clusters correspond to *ca.* 31% of boron present in p-BN, while framework BN corresponds to *ca.* 55% of boron. Therefore, this further suggests that the p-BN material contains a high ratio of pore/defect sites compared to the BN framework. We note that no ^{11}B NMR signals were assigned to B species containing a B−C bond. DFT calculations predict that the ^{11}B isotropic chemical shift increases with the substitution of N for C; replacement of N for C in **BN$_3$** to yield **BN$_2$C** increases the predicted ^{11}B isotropic chemical shift by *ca.* 4 ppm while C_Q remains relatively constant (Figures S18, S19, Tables S3, and S4). Therefore, we infer that either (i) the atomic weight percent of C is very low and/or (ii) C atoms (dopants) within p-BN do not exhibit B−C bonds.

^{11}B−^{15}N Heteronuclear Correlation Solid-State NMR Spectroscopy. The ^{1}H−^{14}N/^{15}N NMR experiments revealed the presence of **NB$_3$**, **NB$_2$H**, **NBH$_2$**, **NBH$_3^+$**, and **NH$_4^+$** species. Ultra-high field 35.2 T ^{11}B NMR experiments suggested that many of the pore/defect sites within p-BN are composed of boron oxide/hydroxide clusters that are connected to the BN framework primarily through **BN$_2$O** species. 2D ^{11}B{^{15}N} D-HMQC experiments were used to probe the spatial connectivity between all boron and nitrogen species. A 2D ^{11}B{^{15}N} D-HMQC spectrum of ^{15}N-enriched p-BN was recorded at B_0 = 14.1 T with 20 kHz MAS and 1.2 ms of total SR4$_1^2$ heteronuclear

dipolar recoupling applied to the ^{15}N spins (Figure 7A, red). A one-bond N−B ^{11}B−^{15}N dipolar coupling constant is *ca.* 1.3 kHz, whereas a three-bond N−B (**N−B−N−B**) ^{11}B−^{15}N dipolar coupling constant is *ca.* 70 Hz. Therefore, only one-bond B−N correlations will be observed in the ^{11}B{^{15}N} D-HMQC NMR experiments. The 2D ^{11}B{^{15}N} D-HMQC spectrum reveals **BN$_3$**, **BN$_2$O**, and **BNO$_2$** species all correlating to bulk **NB$_3$**, further confirming that the **BN$_2$O** and **BNO$_2$** groups reside on the edge of the BN framework. No correlations between boron and the **NB$_2$H**, **NBH$_2$** or **NBH$_3^+$** species were observed, suggesting that the majority of framework BN are boron-terminated. However, when the ^{11}B{^{15}N} D-HMQC was recorded with ^{1}H → ^{11}B CP at the beginning of the experiment, correlations between boron **BN$_3$**, **BN$_2$O**, and **BNO$_2$** species with nitrogen **NB$_3$**, **NB$_2$H**, and **NBH$_2$** were observed (Figure 7A, blue). This observation illustrates that the **NB$_2$H** and **NBH$_2$** species partially terminate the BN framework and are in close spatial proximity to the partially oxidized BN species (**BN$_2$O** and **BNO$_2$**) that terminate and connect the boron oxide/hydroxide cluster to the BN framework. It is worth noting that no correlations between boron and the **NBH$_3^+$** species were observed in any of the ^{11}B{^{15}N} D-HMQC spectra. However, this was likely due to low sensitivity. Indeed, a DNP-SENS ^{15}N{^{11}B} dipolar-dephased RESPDOR (Rotational-Echo Saturation-Pulse DOuble Resonance)[123] spectrum reveals that all ^{15}N species except **NH$_4^+$** contain a directly bonded boron atom, further corroborating the assignment of all ^{15}N NMR signals (Figure 7B). It should be noted that the small extent of dephasing observed in the ^{15}N{^{11}B} dephased spectrum was primarily due to the low achievable ^{11}B RF field of 11 kHz used for the saturation pulse.

Plane-Wave DFT Calculations. Periodic plane-wave DFT calculations utilizing the gauge-including projector-augmented
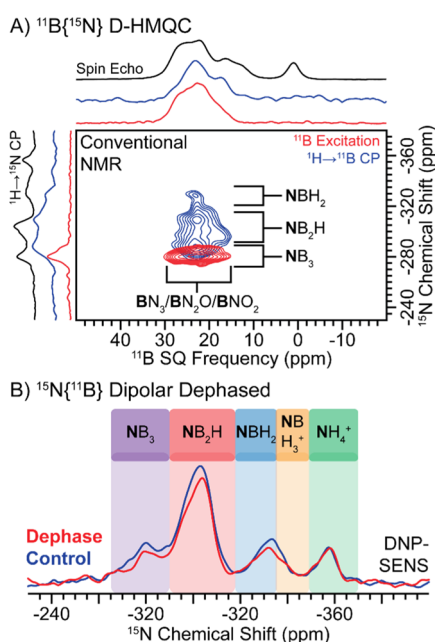
Figure 7. (A) 2D ^{11}B{^{15}N} D-HMQC spectra of ^{15}N-enriched p-BN recorded with ^{1}H → ^{11}B CP (blue, τ_{CP} = 600 μs) or direct excitation of ^{11}B (red) at the start of the experiment. Both spectra were recorded with conventional NMR at ∼300 K and B_0 = 14.1 T with 20 kHz MAS and 1.2 ms of total SR4$_1^2$ heteronuclear dipolar recoupling applied to the ^{15}N spins. An ^{11}B direct excitation spin echo spectrum and ^{1}H → ^{15}N CPMAS (τ_{CP} = 5 ms) spectrum are overlaid above the 2D projections. (B) Comparison of DNP-SENS 1D ^{15}N{^{11}B} RESPDOR spectra recorded with (red, dephased) or without (blue, control) a saturation pulse applied to ^{11}B and 0.8 total ms of first-order R^3 dipolar recoupling applied to the ^{15}N spins. Spectra were acquired at ∼100 K and B_0 = 9.4 T with 10 kHz MAS.

wave (GIPAW) approach is commonly used to calculate NMR parameters, such as chemical shielding tensors, EFG tensors, and

scalar (J-) couplings, to aid in the assignment of NMR signals within inorganic materials.[75,85,124−130] Here, we utilized periodic plane-wave DFT calculations as implemented in CASTEP to build structural models of p-BN and compare the calculated NMR parameters to those determined experimentally. Nine different structural models were calculated containing **BN$_3$**, **BN$_2$O**, **BNO$_2$**, **BO$_3$**, **NB$_3$**, **NB$_2$H**, **NBH$_2$**, and **NBH$_3^+$** functional groups based on our ^{11}B and ^{14}N/^{15}N NMR assignments discussed above (Figures 8, 9, and S20−S28). These models were chosen and constructed because we believe that they represent the most likely combinations of different functional groups and structural motifs based upon the NMR spectra. However, these models are not comprehensive or unique; there are likely other possible structures and configurations which could represent models of p-BN. DFT-calculated ^{15}N chemical shifts for a structural model containing **NB$_3$**, **NB$_2$H**, **NBH$_2$**, and **NBH$_3^+$** functional groups show good agreement with the experimental room temperature ^{1}H → ^{15}N CPMAS spectrum (Figure 8B). In addition, the range and average ^{15}N chemical shifts calculated for all structure models (Figures S20−S28 and Tables S5−S13) show excellent agreement with the experimental spectrum, where the ^{15}N chemical shifts decrease with increasing hydrogenation of nitrogen over the series of **NB$_3$** → **NBH$_3^+$**. Plane-wave DFT-calculated ^{14}N shifts show reasonable agreement with the experimental ^{14}N NMR spectrum (Figure 8C). Here, the range of ^{14}N shifts for **NB$_2$H** and **NBH$_2$** species is significantly larger than that of ^{15}N because variations in the calculated ^{14}N C_Q lead to large differences in the second-order QIS.[97] As discussed above, **NBH$_2$** species are predicted to have significantly larger C_Q than **NB$_2$H** which leads to ^{14}N NMR signals with larger second-order QIS and signal breadths (Figure S11B). Nevertheless, both ^{14}N and ^{15}N plane-wave DFT calculations confirm the ^{14}N/^{15}N NMR assignments discussed above.

The detailed structural characterization of p-BN described here allowed us to build a structural model that was optimized
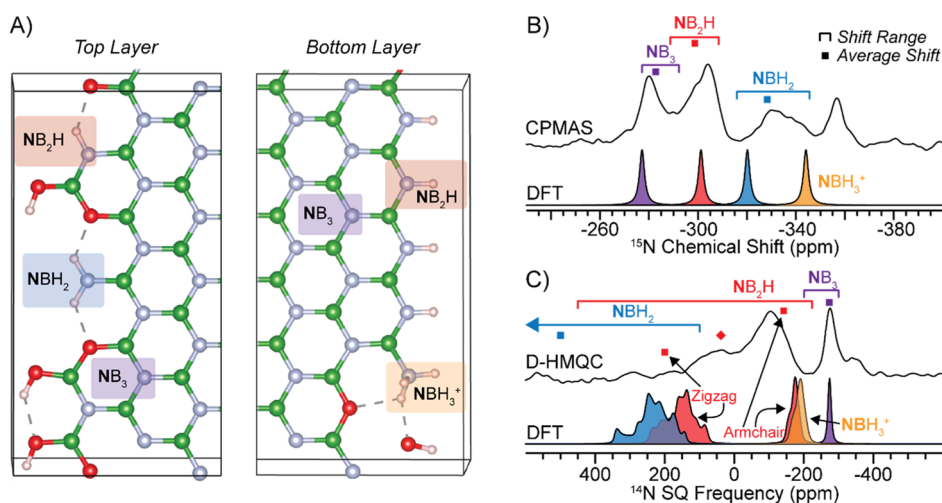

Figure 8. Periodic plane-wave DFT calculations. Silver, green, red, and white atoms correspond to nitrogen, boron, oxygen, and hydrogen, respectively. (A) Structural model of p-BN containing **NB$_2$H**, **NBH$_2$**, and **NBH$_3^+$** edge terminations. The entire structural model is given in Figure S27. DFT-calculated (B) ^{15}N and (C) ^{14}N spectra for different nitrogen species highlighted in (A). Experimental NMR spectra (^{1}H → ^{15}N CPMAS and ^{1}H{^{14}N} D-HMQC ^{14}N projection) are shown above the DFT-calculated spectra. Purple, red, blue, and orange correspond to **NB$_3$**, **NB$_2$H**, **NBH$_2$**, and **NBH$_3^+$**, respectively. The simulated spectra correspond to the highlighted atoms in (A). The **NB$_2$H** ^{15}N spectrum corresponds to the average of the two **NB$_2$H** highlighted atoms in (A). The open rectangles above the spectra illustrate the range in frequencies observed in DFT calculations of many different structural models, and the square indicates the average frequency (see Supporting Information for all calculations). In (C), the diamond represents the average ^{14}N frequency for an **NB$_2$H** group connecting an armchair to zigzag edge.
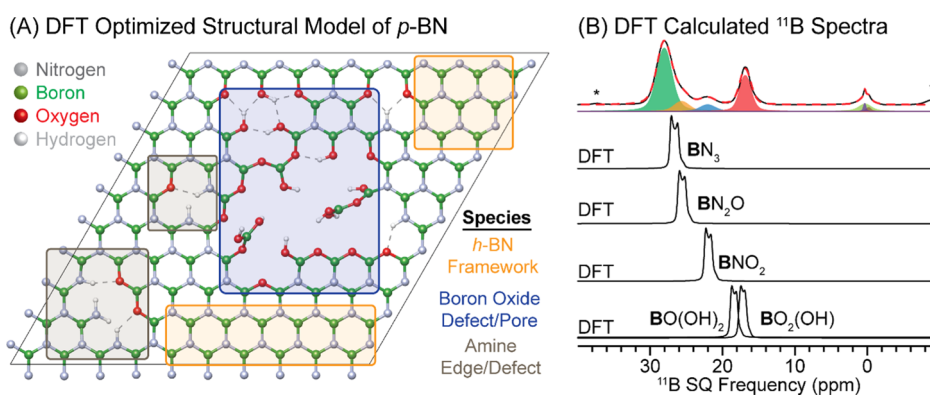
Figure 9. (A) Periodic plane-wave DFT-optimized structural model of p-BN. Silver, green, red, and white atoms correspond to nitrogen, boron, oxygen, and hydrogen, respectively. The highlighted regions illustrate structural units corresponding to the (orange) h-BN framework, (blue) boron oxide pore/defect sites, and (gray) amine edge/defect sites. (B) Comparison of experimental spin echo ^{11}B NMR spectrum and DFT-calculated ^{11}B NMR spectra of (upper to lower) $\mathbf{BN_3}$, $\mathbf{BN_2O}$, $\mathbf{BNO_2}$, and $\mathbf{BO(OH)_2}/\mathbf{BO_2(OH)}$ species within the DFT-optimized structural model shown in (A). The average $\delta_{iso}(^{11}B)$, C_Q, and η of each structural unit was used to simulate the ^{11}B NMR spectra. All DFT-calculated NMR parameters of the structural model is given in Table S13. All spectra/simulations were performed at $B_0 = 35.2$ T with 18 kHz MAS.

through plane-wave DFT calculations (Figure 9A). We note that the structural model is not unique, but it does represent the type of species likely present within p-BN. As determined from ^{1}H$-^{14}$N/^{15}N and ^{11}B$-^{15}$N HETCOR NMR experiments, p-BN contains many nitrogen edge/defect sites mostly composed of $\mathbf{NB_2H}$ and $\mathbf{NBH_2}$ species that are directly attached to the BN framework. We note that there are likely additional $\mathbf{NBH_3}^+$ edge/defect sites in addition to $\mathbf{NH_4}^+$ trapped in the pores and/or between BN layers. Ultra-high field ^{11}B NMR revealed many partially ($\mathbf{BN_2O}$ and $\mathbf{BNO_2}$) and fully ($\mathbf{BO_3}$ and $\mathbf{BO_4}^-$) oxidized/hydrolyzed boron species. Most importantly, the ^{11}B DQ−SQ data revealed that many of the pore and defect sites are composed of boron oxide/hydroxide clusters that are directly attached to the BN framework through $\mathbf{BN_2O}$ species. DFT-calculated ^{11}B NMR spectra of the proposed structural model are in excellent agreement with the experimental data, where $\delta_{iso}(^{11}B)$ decreases with increasing oxidation of $\mathbf{BN_3}$ (i.e., $\mathbf{BN_3} \rightarrow \mathbf{BO_3}$, Figure 9B and Table S13). Therefore, we propose that many of the pore and defect sites within p-BN are composed of boron oxide/hydroxide clusters, but there are other amine and boron oxide/hydroxide edge/defect sites throughout the material that likely compose a smaller fraction of the defect/edge and pores sites.

■ CONCLUSIONS

In this contribution, high-resolution multinuclear solid-state NMR spectroscopy and plane-wave DFT calculations enabled the determination of atomic-level structure within mesoporous h-BN (p-BN). ^{1}H$-^{15}$N HETCOR experiments on ^{15}N-enriched p-BN recorded with either conventional NMR at room temperature or DNP-SENS at ca. 100 K revealed the presence of $\mathbf{NB_3}$, $\mathbf{NB_2H}$, $\mathbf{NBH_2}$, $\mathbf{NBH_3}^+$, and $\mathbf{NH_4}^+$ species. The identification of $\mathbf{NB_3}$, $\mathbf{NB_2H}$, and $\mathbf{NBH_3}^+$ was also confirmed by recording a 2D ^{1}H{^{14}N} HETCOR spectrum with fast MAS. Ultra-high field 35.2 T ^{11}B NMR spectroscopy quantitatively probes all boron species within p-BN allowing for the identification of ^{11}B NMR signals attributed to $\mathbf{BN_3}$, $\mathbf{BN_2O_x(OH)_{1-x}}$ ($x = 0-1$), $\mathbf{BNO_x(OH)_{2-x}}$ ($x = 0-2$), $\mathbf{BO_x(OH)_{3-x}}$ ($x = 0-3$), and $\mathbf{BO_x(OH)_{4-x}}^-$ ($x = 0-4$) sites. Most importantly, 2D ^{11}B dipolar DQ−SQ homonuclear correlation spectra revealed that pore/defect sites are composed of boron oxide/hydroxide clusters which are homogeneously

distributed throughout the BN framework and connected via $\mathbf{BN_2O}$ units. 1D and 2D ^{11}B{^{15}N} HETCOR NMR experiments further confirmed the assignment of all NMR signals. Lastly, plane-wave DFT calculations were used to construct structural models of p-BN and calculate ^{11}B and $^{14/15}$N NMR parameters. DFT-calculated ^{15}N chemical shifts of nine different structural models containing $\mathbf{NB_3}$, $\mathbf{NB_2H}$, $\mathbf{NBH_2}$, and/or $\mathbf{NBH_3}^+$ functional groups showed excellent agreement with the experimental ^{15}N CPMAS spectra. In particular, the ^{15}N chemical shift decreases with increasing hydrogenation of $\mathbf{NB_3}$ ($\mathbf{NB_3} \rightarrow \mathbf{NBH_3}^+$). In addition, DFT-calculated ^{14}N and ^{11}B shifts also showed good agreement with the experimental spectra. The identification of all boron and nitrogen species present within p-BN by high-resolution multinuclear solid-state NMR spectroscopy enabled us to build a proposed structural model that was optimized through plane-wave DFT calculations. This model shows that many of the pore and defect sites within p-BN are composed of boron oxide/hydroxide clusters, but there are other amine and boron oxide/hydroxide edge/defect sites throughout the material that likely compose a smaller fraction of the overall defect/edge and pores sites.

The observation that many of the pore and edge/defect sites are primarily composed of boron oxide/hydroxide clusters suggest that boron oxidation occurs readily and often during BN framework formation (during calcination) and is a leading cause for the formation of such highly defective materials with high SSAs. With such a large fraction of boron oxide/hydroxide clusters connected to the BN framework, we speculate that these species likely play an important role in the overall chemical adsorption properties of p-BN materials. Furthermore, the detailed structure determination of the pore and edge/defect sites within p-BN should further enable the rational design and development of next-generation adsorption materials. The functionalization of p-BN materials should be easier to implement with knowledge of the molecular structure of the pore and edge sites. For example, chemical functionalization strategies could be designed that consider the chemistry of boron oxide/hydroxide and/or amine groups. We anticipate that chemical modification of p-BN could be a strategy to tune adsorption towards specific substrates.

■ EXPERIMENTAL SECTION

Materials. Porous BN was synthesized following previously published methods.[65,68] In general, boric acid (H_3BO_3, Certified ACS Reagent, Fischer Scientific), urea (CH_4N_2O, molecular biology grade, Sigma-Aldrich), and melamine ($C_3H_6N_6$, ACS Reagent, 99% Alfa Aesar), with a 1:1 molar ratio of boric acid to melamine and a 1:5 molar ratio of boric acid to urea, were ground together in a mortar for 5 min to form a homogenous powder. For the ^{15}N-enriched material, natural isotopic abundance urea was replaced with ^{15}N-labeled urea (98% ^{15}N, Sigma-Aldrich). The mixture was collected, layered thinly in a quartz boat (35 mg), and placed in a horizontal tube furnace with 1 inch diameter quartz tube. The sample was purged with Ar gas with a flow rate of 250 mL/min for 2 h at room temperature and subsequently heated to 1050 °C at a ramping rate of 10 °C/min and a decreased flow rate of 50 mL/min. The sample was held at 1050 °C for 3.5 h and allowed to cool to room temperature. Porous BN was collected from the quartz boat.

We note that the reaction to produce porous BN gives a low yield. Loading the quartz boat with too much starting material as a thick layer yields a gray material, indicative of high carbon content. To produce pure, carbon-free materials, a thin layer of starting material was coated on the bottom of the quartz boat. A typical synthesis yielded *ca.* 3–4 mg of porous BN, completely white in color. The yield did not increase when the sample was purged with Ar or N_2 gas at a low flow rate of 25 mL/min for 2 h at room temperature and subsequently heated to 1050 °C at a ramping rate of 10 °C/min and a decreased flow rate of 5 mL/min.

Electron Microscopy. SEM images were acquired on a Teneo SEM (Thermo Fisher Scientific). TEM study was performed at 200 kV on a probe aberration corrected Titan Themis TEM (Thermo Fisher Scientific) with a Super-X EDS detector and Quantum 965 GIF system. STEM–EDS and STEM–EELS were performed with a probe current of 150 and 40 pA, respectively.

Fourier Transform Infrared Spectroscopy. A FTIR spectroscopy spectrum was collected using an Agilent Cary 630 FTIR equipped with an attenuated total reflectance (ATR) attachment containing a diamond crystal. About 5 mg of sample was pressed between the stand and the ATR crystal. All spectra were obtained at a resolution of 2 cm^{-1} (from 700 to 4000 cm^{-1}) under atmospheric pressure.

Density Functional Theory. Periodic plane-wave density functional theory (DFT) calculations were performed with the GIPAW[131] approach as implemented in CASTEP version 2017 R2.[132] NMR calculations and geometry optimizations utilized the generalized gradient approximation with the Perdew–Burke–Ernzerhof exchange–correlation functional,[133] Tkatchenko–Scheffler dispersion corrections,[134] On-the-fly ultrasoft pseudopotentials,[135,136] zeroth-order regular approximation (ZORA) relativistic treatments,[137] a 0.07 Å^{-1} k-point spacing and a 630 eV kinetic energy cutoff. DFT-calculated ^{11}B and ^{14}N/^{15}N isotropic chemical shieldings (σ) were converted to isotropic chemical shifts (δ) using our previously published calibration curves.[75] DFT-calculated ^{11}B quadrupolar coupling constants (C_Q) and asymmetry parameters (η) were slightly corrected using our previously published calibration curves.[75]

All porous h-BN structural models were initially constructed from structurally modified supercells (typically ranging from $6 \times 6 \times 1$ to $10 \times 10 \times 1$) of the previously published single-crystal X-ray diffraction structure of h-BN.[138] Structural models containing "edge terminations" were built by cleaving the crystal structure of h-BN along the {0–10} plane. Structural models containing "defects/pores" were built by removing interior sheet atoms and keeping the entire structure periodic. We note that some models were constructed as either a single sheet with a *ca.* 6 Å vacuum between additional sheets or as an infinitely stacked "bulk-like" structure with a layer spacing of *ca.* 3.5 Å. However, our previous work on h-BN nanosheets showed that the interlayer spacing (*i.e.*, single sheet *vs* bulk-like structure) had no impact on the DFT-calculated NMR parameters.[75] The crystal files for all structural models are available in the Supporting Information.

Solid-State NMR Numerical Simulations. Numerical simulations of $^{15}N\{^1H\}$ SLF and DIPSHIFT solid-state NMR spectroscopy experiments were performed using SIMPSON v4.2.1.[139−141] All simulations were performed with the same magnetic field strength, MAS frequency, and pulses (*i.e.*, pulse duration and RF field) as the experimental data. All simulations were performed with the rep168 crystal file, 8 gamma angles, and a (DIPSHIFT) 1 μs or (SLF) 1.5 μs maximum time duration, where the Hamiltonian was considered time independent. Larger crystal files, more gamma angles, and smaller time durations, where the Hamiltonian is considered time independent, were performed for a select number of simulations to ensure the simulations fully converged with the above-mentioned parameters. $^{15}N\{^1H\}$ SLF and DIPSHIFT numerical simulations used to fit the experimental curves for the ^{15}N NMR signals assigned to (−305 ppm) **N**B_2H, (−333 ppm) **N**BH_2, and (−340 ppm) **N**BH_3^+ utilized a two (^1H−^{15}N), three ($^1H_2$−^{15}N), or four ($^1H_3$−^{15}N) spin system to accurately represent the species probed. Euler angles relating ^1H and ^{15}N CSA and dipolar tensors were obtained from plane-wave DFT calculations. $^{15}N\{^1H\}$ SLF and DIPSHIFT numerical simulation files used to fit the experimental curves for the ^{15}N NMR signals assigned to (−305 ppm) **N**B_2H, (−333 ppm) **N**BH_2, and (−340 ppm) **N**BH_3^+ are available in the Supporting Information.

General Solid-State NMR Spectroscopy. All experimental parameters (magnetic field strength, MAS rate, recycle delay, number of scans, t_1 TD points, t_1 dwell (Δt_1), CP/recoupling duration, and total experimental times) are given in Table S14. All ^1H and ^{11}B longitudinal relaxation constants (T_1) were measured using a saturation recovery experiment. All NMR spectra were processed using either Topspin 3.6.1 (Avance II or III data) or Topspin 4.0.7 (Avance NEO data). Analytical fits of NMR spectra were performed using either the solid lineshape analysis (sola) module as implemented in Topspin or the ssNake NMR software.[142] A schematic illustration of all pulse sequences is given in Figure S29.

Solid-State NMR Spectroscopy at 9.4 T. Solid-state NMR spectroscopy experiments were performed on a 9.4 T ($\nu_0(^1H)$ = 400 MHz) Bruker wide-bore magnet equipped with a Bruker AVANCE III HD console and either a 2.5 mm HXY or 1.3 mm HX magic-angle spinning (MAS) NMR probe. A 20 pF shunt capacitor was placed in parallel with the X-channel of the 9.4 T 1.3 mm HX MAS NMR probe in order to tune the X channel of the probe to ^{14}N (∼28.9 MHz). ^1H chemical shifts were referenced to neat tetramethylsilane (TMS) with adamantane ($\delta_{iso}(^1H)$ = 1.82 ppm) as a secondary chemical shift reference. ^{11}B, ^{14}N and ^{15}N shifts were indirectly referenced to (^{11}B) $BF_3{\cdot}Et_2O$ or ($^{14/15}N$) CH_3NO_2 using previously published IUPAC-recommended relative NMR frequencies.[143]

All ^1H $\pi/2$ and π pulse lengths were 2.5 μs and 5 μs in duration, corresponding to a 100 kHz RF field. ^{11}B $\pi/2$ and π pulse lengths were 5 μs and 10 μs in duration, corresponding to a 25 kHz RF field and 50 kHz CT nutation frequency. ^{15}N $\pi/2$ and π pulse lengths were either (1.3 mm probe; 50 kHz MAS) 4.125 and 8.25 μs or (2.5 mm probe; 25 kHz MAS) 5.15 and 10.3 μs in duration. ^1H → ^{15}N CP was achieved at 25 kHz MAS with simultaneous ^1H (85−100% ramp) and ^{15}N spin-lock pulses with RF fields of *ca.* 64 kHz and 40 kHz, respectively. ^1H → ^{15}N CP was achieved at 45 kHz MAS with simultaneous ^1H (90−100% ramp) and ^{15}N spin-lock pulses with RF fields of *ca.* 66 kHz and 20 kHz, respectively. A 2D ^1H → ^{15}N CP-HETCOR spectrum was recorded with 25 kHz MAS and eDUMBO$_{1−22}$ ^1H homonuclear dipolar decoupling (100 kHz RF field) during the indirect acquisition of ^1H.[78] $^{15}N\{^1H\}$ symmetry-based recoupling separated-local field (SLF) experiments were performed with either ^{15}N detection and 25 kHz MAS or ^1H detection (^{15}N → ^1H backward CP) and 45 kHz MAS.[83,84] Both $^{15}N\{^1H\}$ SLF experiments utilized the symmetry-based SR4$_2^1$ heteronuclear dipolar recoupling scheme applied to the ^1H spins.[144] $^1H\{^{14}N\}$ dipolar HMQC experiments were performed with the symmetry-based SR4$_1^2$ heteronuclear dipolar recoupling scheme applied to the ^1H spins and a 20 μs (1 rotor period; 50 kHz MAS) ^{14}N excitation pulse length with a *ca.* 37 kHz RF field.[90,92−94,96,144] ^{11}B split-t_1 triple-quantum multiple-quantum MAS (3Q-MQMAS) experiments were performed with 3Q excitation and 1Q reconversion pulse lengths of 2.04 μs and 0.6 μs and an RF field of *ca.* 225 kHz.[145−147] High-power 100 kHz ^1H RF field of SPINAL-64 heteronuclear decoupling was applied during the direct and indirect detection of ^{15}N at 25 kHz

MAS.[148] Low-power HORROR (RF field = 0.5 × MAS rate) continuous-wave ^{1}H heteronuclear decoupling was performed during the direct and indirect acquisition of ^{11}B or ^{15}N at MAS rates greater than or equal to 45 kHz.

Solid-State NMR Spectroscopy at 14.1 T. Solid-state NMR spectroscopy experiments were performed on a 14.1 T ($\nu_0(^1$H) = 600 MHz) Bruker wide-bore magnet equipped with a Bruker Avance II console and a 2.5 mm HXY MAS NMR probe. ^{1}H chemical shifts were referenced to neat TMS with adamantane [$\delta_{iso}(^1$H) = 1.82 ppm] as a secondary chemical shift reference. ^{11}B and ^{15}N shifts were indirectly referenced to (^{11}B) BF$_3$·Et$_2$O and (^{15}N) CH$_3$NO$_2$ using previously published IUPAC-recommended relative NMR frequencies.[143]

All ^{1}H $\pi/2$ and π pulse lengths were 2.5 and 5 μs in duration, corresponding to a 100 kHz RF field. ^{11}B $\pi/2$ and π pulse lengths were 8 and 16 μs in duration, corresponding to a 15.625 kHz RF field and 31.25 kHz CT nutation frequency. ^{15}N $\pi/2$ and π pulse lengths were 6 and 12 μs in duration, corresponding to a 41.67 kHz RF field. ^{1}H → ^{11}B CP was achieved at 20 kHz MAS with simultaneous ^{1}H (90−100% ramp) and ^{11}B spin-lock pulses with RF fields of *ca.* 48 kHz and 5 kHz, respectively. ^{11}B{^{15}N} D-HMQC experiments were performed either with or without ^{1}H → ^{11}B CP at the beginning of the experiment and 20 kHz MAS. 40 kHz RF field of the symmetry-based SR4$_1^2$ heteronuclear dipolar recoupling scheme was applied to the ^{15}N spins to re-introduce the ^{11}B−^{15}N dipolar interaction.[144]

Solid-State NMR Spectroscopy at 19.6 T. Solid-State NMR spectroscopy experiments were performed on a 19.6 T ($\nu_0(^1$H) = 833 MHz) magnet equipped with a Bruker AVANCE NEO console and Low-E 3.2 mm HX MAS NMR probe. ^{1}H and ^{11}B chemical shifts were indirectly referenced using the ^{17}O shift of tap water (δ_{iso} = 2.825 ppm) and IUPAC-recommended relative NMR frequencies for ^{1}H (neat TMS) and ^{11}B (BF$_3$·Et$_2$O).[143]

^{1}H $\pi/2$ and π pulse lengths were 5 and 10 μs in duration, corresponding to a 50 kHz RF field. ^{11}B CT-selective $\pi/2$ and π pulse lengths were 5 and 10 μs in duration, corresponding to 25 kHz RF and 50 kHz CT-nutation frequency. ^{11}B{^{1}H} D-HMQC experiments were performed with the symmetry-based SR4$_1^2$ heteronuclear dipolar recoupling scheme applied to the ^{1}H spins.[144] ^{11}B triple-quantum multiple-quantum MAS (3Q-MQMAS) experiments were performed with 3Q excitation and 1Q reconversion pulse lengths of 7.1 and 2.3 μs and an RF field of *ca.* 89 kHz.[145−147] ^{11}B single-quantum−single-quantum (SQ−SQ) spin-diffusion homonuclear correlation experiments were performed with a basic three pulse sequence consisting of a spin-diffusion period, while the ^{11}B spins are aligned with the magnetic field. ^{11}B dipolar DQ−SQ homonuclear correlation experiments were performed with the BR2$_2^1$ homonuclear dipolar recoupling sequence to generate DQ coherence directly from ^{11}B Z-magnetization.[117] A CT-selective π pulse was applied during t_1 evolution to ensure only CT DQ coherence was selected during phase cycling.[115] Each π pulse in the BR2$_2^1$ block was 1 rotor cycle in duration (71.43 μs@14 kHz MAS). 50 kHz ^{1}H RF field of SPINAL-64 heteronuclear decoupling was applied during the direct acquisition of ^{11}B.[148]

Solid-State NMR Spectroscopy at 35.2 T. Solid-State NMR spectroscopy experiments were performed on a 36 T SCH magnet operating at a field strength of 35.2 T ($\nu_0(^1$H) = 1500 MHz). The 36 T SCH magnet was designed, built, and is stationed at the National High Magnetic Field Laboratory (NHMFL) in Tallahassee, FL.[102] The 36 T SCH magnet is equipped with a Bruker AVANCE NEO console and a 3.2 mm low-E HX MAS NMR probe designed and built at the NHMFL. The magnetic field strength of the SCH NMR magnet is regulated with a magnetic flux sensor and ^{7}Li NMR signal from an external lock sample that is located 9 mm away from the NMR sample.[102] ^{1}H chemical shifts observed in the 2D ^{11}B{^{1}H} D-HMQC were indirectly referenced from the 2D ^{11}B{^{1}H} D-HMQC spectrum recorded at B_0 = 19.6 T. ^{11}B chemical shifts were initially indirectly referenced using ^{2}H shifts of D$_2$O (δ_{iso} = 4.7 ppm) and the previously published IUPAC-recommended ^{11}B relative NMR frequency (BF$_3$·Et$_2$O).[143] To ensure accurate ^{11}B shifts are reported, the ^{11}B shifts were slightly corrected by calibrating the 4-coordinate BO$_4^−$ ^{11}B NMR signal in a direct excitation spin echo experiment to that observed in a direct excitation spin echo experiment at B_0 = 19.6 T (δ = 0.25 ppm) because there is essentially no

QIS for sites with C_Q < 0.5 MHz at these field strengths.[76] All subsequent ^{11}B spectra recorded on the SCH were then referenced based on the corrected ^{11}B spin echo NMR spectrum. This additional ^{11}B chemical shift correction was implemented because the field stability is within only *ca.* 1 ppm after sample changes (where the magnetic field must be ramped down from 35.2 to 0 T, and then back to 35.2 T) and the homogeneity is *ca.* 1 ppm over 1 cm^3. We note that there can be field drift up to *ca.* 0.5 ppm during an NMR experiment, which may broaden the NMR signal. Therefore, we anticipate that the reported ^{11}B shifts have an uncertainty of *ca.* 0.5 ppm due to magnetic field drift and the ^{11}B shift correction mentioned above. However, the small uncertainty in the reported ^{11}B shifts do not affect the analysis.

^{1}H $\pi/2$ pulse lengths were 5.4 μs in duration, corresponding to a *ca.* 46 kHz RF field. ^{11}B CT-selective $\pi/2$ pulse lengths were either 3 μs (^{11}B spin echo), 12 μs (^{11}B{^{1}H} D-HMQC), or 20 μs (^{11}B DQ−SQ) in duration. A quantitative $\pi/6$ single-pulse ^{11}B NMR spectrum was recorded with a pulse duration of 1 μs (*ca.* 41.7 kHz RF field) and recycle delay of 100 s. ^{11}B{^{1}H} D-HMQC experiments were performed with the symmetry-based SR4$_1^2$ heteronuclear dipolar recoupling scheme applied to the ^{1}H spins.[144] ^{11}B dipolar DQ−SQ homonuclear correlation experiments were performed with the BR2$_2^1$ homonuclear dipolar recoupling sequence to generate DQ coherence directly from ^{11}B Z-magnetization.[117] A CT-selective π pulse was applied during t_1 evolution to ensure only CT DQ coherence was selected during phase cycling.[115] Each π pulse in the BR2$_2^1$ block was 1 rotor cycle in duration (55.56 μs@18 kHz MAS). ^{11}B DQ−SQ experiments were recorded with a t_1 dwell (Δt_1) equal to half a rotor period (∼27.8 μs@18 kHz MAS). A sign reversal of the NMR signal occurs when the Δt_1 is equal to a half of a rotor cycle because the dipolar Hamiltonian depends on the rotor rotation angle under BR2$_2^1$ homonuclear dipolar recoupling.[122] 50 kHz ^{1}H RF field of SPINAL-64 heteronuclear decoupling was applied throughout the entire ^{11}B DQ−SQ experiment.[148] Rotor-assisted population transfer was performed at the beginning of all ^{11}B{^{1}H} D-HMQC and ^{11}B DQ−SQ experiments with a WURST pulse applied 250 kHz off-resonance and with a frequency sweep equal to the MAS rate (18 kHz MAS).[149,150]

Dynamic Nuclear Polarization at 9.4 T. DNP-enhanced solid-state NMR spectroscopy was performed on a 9.4 T 400 MHz/263 GHz spectrometer equipped with a Bruker AVANCE III console and 3.2 mm HXY DNP MAS NMR probe. ^{15}N-enriched p-BN was prepared for DNP by mixing *ca.* 4 mg of p-BN with 5 μL of 16 mM TEKPol in 1,1,2,2-tetrachloroethane (TCE). The mixture was then packed into a 3.2 mm sapphire NMR rotor, sealed with a Teflon plug, and capped with a zirconia drive cap. Before performing NMR experiments, the sample was degassed by freezing the sample in the NMR probe (∼100 K) and then ejecting the rotor into the sample catcher for *ca.* 4 min (∼295 K) before re-inserting the rotor into the NMR probe (∼100 K). ^{1}H chemical shifts were referenced to neat TMS with frozen TCE (δ_{iso} = 6.2 ppm) as a secondary external shift reference. ^{11}B and ^{15}N shifts were indirectly referenced to (^{11}B) BF$_3$·Et$_2$O and (^{15}N) CH$_3$NO$_2$ using previously published IUPAC-recommended relative NMR frequencies.[143]

^{1}H−^{15}N double resonance NMR experiments were performed with the DNP MAS probe in the double resonance ^{1}H−Y mode and a 39 pF shunt capacitor attached in parallel to the Y-channel. ^{1}H $\pi/2$ and π pulse lengths were 2.5 and 5 μs in duration, respectively, corresponding to a 100 kHz RF field. ^{15}N $\pi/2$ and π pulse lengths were 5 and 10 μs in duration, respectively, corresponding to a 50 kHz RF field. ^{1}H → ^{15}N CP was achieved at 10 kHz MAS with simultaneous ^{1}H (90−100% ramp) and ^{15}N spin-lock pulses with RF fields of *ca.* 54 kHz and 32 kHz, respectively. ^{1}H → ^{15}N CP was achieved at 3.846 kHz MAS with simultaneous ^{1}H (90−100% ramp) and ^{15}N spin-lock pulses with RF fields of *ca.* 42 kHz and 32 kHz, respectively. ^{15}N{^{1}H} DIPSHIFT experiments were performed with 3.846 kHz MAS.[87] Frequency-switched Lee−Golberg pulses were 10 μs in duration with a *ca.* 81.7 kHz RF field.[151,152] 100 kHz ^{1}H RF field of SPINAL-64 heteronuclear decoupling was applied during the direct acquisition of ^{15}N.[148]

^{1}H−^{11}B−^{15}N triple resonance experiments were performed with the DNP MAS probe in triple resonance mode and a 22 pF shunt capacitor

attached in parallel to the Y channel. ^{15}N $\pi/2$ and π pulse lengths were 13.25 and 26.5 μs in duration, corresponding to a *ca.* 19 kHz RF field. ^{1}H → ^{15}N CP was achieved at 10 kHz MAS with simultaneous ^{1}H (90−100% ramp) and ^{15}N spin-lock pulses with RF fields of *ca.* 41 and 19 kHz, respectively. ^{15}N{^{11}B} RESPDOR experiments were performed with first order R^3 applied to the ^{15}N spins (10 kHz RF field@10 kHz MAS) and a 150 μs (1.5 rotor period) ^{11}B saturation pulse with a *ca.* 11 kHz RF field. 100 kHz ^{1}H RF field of SPINAL-64 heteronuclear decoupling was applied throughout the entire ^{15}N{^{11}B} RESPDOR experiment.[148]

■ ASSOCIATED CONTENT

Ⓢ Supporting Information

The Supporting Information is available free of charge at https://pubs.acs.org/doi/10.1021/acs.chemmater.1c03791.

> Additional microscopy images, FTIR spectra, solid-state NMR spectra, numerical simulations, DFT-calculated structures, DFT-calculated NMR parameters, NMR experimental parameters, and illustration of all NMR pulse sequences (PDF)
>
> Porous BN DFT files (ZIP)
>
> SIMPSON input files (ZIP)

■ AUTHOR INFORMATION

Corresponding Authors

Wenyu Huang − *US Department of Energy, Ames Laboratory, Ames, Iowa 50011, United States; Department of Chemistry, Iowa State University, Ames, Iowa 50011, United States;* ⓞ orcid.org/0000-0003-2327-7259; Phone: 515-294-7084; Email: whuang@iastate.edu

Aaron J. Rossini − *US Department of Energy, Ames Laboratory, Ames, Iowa 50011, United States; Department of Chemistry, Iowa State University, Ames, Iowa 50011, United States;* ⓞ orcid.org/0000-0002-1679-9203; Phone: 515-294-8952; Email: arossini@iastate.edu

Authors

Rick W. Dorn − *US Department of Energy, Ames Laboratory, Ames, Iowa 50011, United States; Department of Chemistry, Iowa State University, Ames, Iowa 50011, United States*

Patrick M. Heintz − *US Department of Energy, Ames Laboratory, Ames, Iowa 50011, United States; Department of Chemistry, Iowa State University, Ames, Iowa 50011, United States*

Ivan Hung − *National High Magnetic Field Laboratory (NHMFL), Tallahassee, Florida 32310, United States;* ⓞ orcid.org/0000-0001-8916-739X

Kuizhi Chen − *National High Magnetic Field Laboratory (NHMFL), Tallahassee, Florida 32310, United States*

Jin-Su Oh − *US Department of Energy, Ames Laboratory, Ames, Iowa 50011, United States*

Tae-Hoon Kim − *US Department of Energy, Ames Laboratory, Ames, Iowa 50011, United States*

Lin Zhou − *US Department of Energy, Ames Laboratory, Ames, Iowa 50011, United States;* ⓞ orcid.org/0000-0003-2286-6510

Zhehong Gan − *National High Magnetic Field Laboratory (NHMFL), Tallahassee, Florida 32310, United States;* ⓞ orcid.org/0000-0002-9855-5113

Complete contact information is available at:
https://pubs.acs.org/10.1021/acs.chemmater.1c03791

Notes

The authors declare no competing financial interest.
Raw NMR data is available for download at DOI: 10.5281/zenodo.5510264.

■ REFERENCES

(1) Wang, S.; Peng, Y. Natural zeolites as effective adsorbents in water and wastewater treatment. *Chem. Eng. J.* **2010**, *156*, 11−24.

(2) Fu, F.; Wang, Q. Removal of heavy metal ions from wastewaters: A review. *J. Environ. Manage.* **2011**, *92*, 407−418.

(3) Ali, I.; Asim, M.; Khan, T. A. Low cost adsorbents for the removal of organic pollutants from wastewater. *J. Environ. Manage.* **2012**, *113*, 170−183.

(4) Gupta, S.; Tai, N.-H. Carbon materials as oil sorbents: a review on the synthesis and performance. *J. Mater. Chem. A* **2016**, *4*, 1550−1565.

(5) Lei, W.; Portehault, D.; Liu, D.; Qin, S.; Chen, Y. Porous boron nitride nanosheets for effective water cleaning. *Nat. Commun.* **2013**, *4*, 1777.

(6) Li, J.-R.; Kuppler, R. J.; Zhou, H.-C. Selective gas adsorption and separation in metal-organic frameworks. *Chem. Soc. Rev.* **2009**, *38*, 1477−1504.

(7) Choi, S.; Drese, J. H.; Jones, C. W. Adsorbent Materials for Carbon Dioxide Capture from Large Anthropogenic Point Sources. *ChemSusChem* **2009**, *2*, 796−854.

(8) Furukawa, H.; Cordova, K. E.; O'Keeffe, M.; Yaghi, O. M. The Chemistry and Applications of Metal-Organic Frameworks. *Science* **2013**, *341*, 1230444.

(9) Sevilla, M.; Mokaya, R. Energy storage applications of activated carbons: supercapacitors and hydrogen storage. *Energy Environ. Sci.* **2014**, *7*, 1250−1280.

(10) Seo, J. S.; Whang, D.; Lee, H.; Jun, S. I.; Oh, J.; Jeon, Y. J.; Kim, K. A homochiral metal-organic porous material for enantioselective separation and catalysis. *Nature* **2000**, *404*, 982−986.

(11) Liu, Y.; Xuan, W.; Cui, Y. Engineering Homochiral Metal-Organic Frameworks for Heterogeneous Asymmetric Catalysis and Enantioselective Separation. *Adv. Mater.* **2010**, *22*, 4112−4135.

(12) Adil, K.; Belmabkhout, Y.; Pillai, R. S.; Cadiau, A.; Bhatt, P. M.; Assen, A. H.; Maurin, G.; Eddaoudi, M. Gas/vapour separation using ultra-microporous metal-organic frameworks: insights into the structure/separation relationship. *Chem. Soc. Rev.* **2017**, *46*, 3402−3430.

(13) Frackowiak, E.; Béguin, F. Carbon materials for the electrochemical storage of energy in capacitors. *Carbon* **2001**, *39*, 937−950.

(14) Zhang, L. L.; Zhao, X. S. Carbon-based materials as supercapacitor electrodes. *Chem. Soc. Rev.* **2009**, *38*, 2520−2531.

(15) Zhu, Y.; Murali, S.; Stoller, M. D.; Ganesh, K. J.; Cai, W.; Ferreira, P. J.; Pirkle, A.; Wallace, R. M.; Cychosz, K. A.; Thommes, M.; Su, D.; Stach, E. A.; Ruoff, R. S. Carbon-Based Supercapacitors Produced by Activation of Graphene. *Science* **2011**, *332*, 1537.

(16) Corma, A. From Microporous to Mesoporous Molecular Sieve Materials and Their Use in Catalysis. *Chem. Rev.* **1997**, *97*, 2373−2420.

(17) Huh, S.; Chen, H.-T.; Wiench, J. W.; Pruski, M.; Lin, V. S.-Y. Cooperative Catalysis by General Acid and Base Bifunctionalized Mesoporous Silica Nanospheres. *Angew. Chem., Int. Ed.* **2005**, *44*, 1826−1830.

(18) Lee, J.; Farha, O. K.; Roberts, J.; Scheidt, K. A.; Nguyen, S. T.; Hupp, J. T. Metal-organic framework materials as catalysts. *Chem. Soc. Rev.* **2009**, *38*, 1450−1459.

(19) Yang, S.; Zhi, L.; Tang, K.; Feng, X.; Maier, J.; Müllen, K. Efficient Synthesis of Heteroatom (N or S)-Doped Graphene Based on Ultrathin Graphene Oxide-Porous Silica Sheets for Oxygen Reduction Reactions. *Adv. Funct. Mater.* **2012**, *22*, 3634−3640.

(20) Liu, J.; Chen, L.; Cui, H.; Zhang, J.; Zhang, L.; Su, C.-Y. Applications of metal-organic frameworks in heterogeneous supramolecular catalysis. *Chem. Soc. Rev.* **2014**, *43*, 6011−6061.

(21) Lian, G.; Zhang, X.; Zhang, S.; Liu, D.; Cui, D.; Wang, Q. Controlled fabrication of ultrathin-shell BN hollow spheres with excellent performance in hydrogen storage and wastewater treatment. *Energy Environ. Sci.* **2012**, *5*, 7072−7080.

(22) Li, J.; Xiao, X.; Xu, X.; Lin, J.; Huang, Y.; Xue, Y.; Jin, P.; Zou, J.; Tang, C. Activated boron nitride as an effective adsorbent for metal ions and organic pollutants. *Sci. Rep.* **2013**, *3*, 3208.

(23) Li, J.; Lin, J.; Xu, X.; Zhang, X.; Xue, Y.; Mi, J.; Mo, Z.; Fan, Y.; Hu, L.; Yang, X.; Zhang, J.; Meng, F.; Yuan, S.; Tang, C. Porous boron nitride with a high surface area: hydrogen storage and water treatment. *Nanotechnology* **2013**, *24*, 155603.

(24) Xue, L.; Lu, B.; Wu, Z.-S.; Ge, C.; Wang, P.; Zhang, R.; Zhang, X.-D. Synthesis of mesoporous hexagonal boron nitride fibers with high surface area for efficient removal of organic pollutants. *Chem. Eng. J.* **2014**, *243*, 494−499.

(25) Liu, D.; Lei, W.; Qin, S.; Chen, Y. Template-Free Synthesis of Functional 3D BN architecture for removal of dyes from water. *Sci. Rep.* **2014**, *4*, 4453.

(26) Li, J.; Huang, Y.; Liu, Z.; Zhang, J.; Liu, X.; Luo, H.; Ma, Y.; Xu, X.; Lu, Y.; Lin, J.; Zou, J.; Tang, C. Chemical activation of boron nitride fibers for improved cationic dye removal performance. *J. Mater. Chem. A* **2015**, *3*, 8185−8193.

(27) Liu, D.; Lei, W.; Qin, S.; Klika, K. D.; Chen, Y. Superior adsorption of pharmaceutical molecules by highly porous BN nanosheets. *Phys. Chem. Chem. Phys.* **2016**, *18*, 84−88.

(28) Lin, J.; Xu, L.; Huang, Y.; Li, J.; Wang, W.; Feng, C.; Liu, Z.; Xu, X.; Zou, J.; Tang, C. Ultrafine porous boron nitride nanofibers synthesized via a freeze-drying and pyrolysis process and their adsorption properties. *RSC Adv.* **2016**, *6*, 1253−1259.

(29) Li, J.; Jin, P.; Dai, W.; Wang, C.; Li, R.; Wu, T.; Tang, C. Excellent performance for water purification achieved by activated porous boron nitride nanosheets. *Mater. Chem. Phys.* **2017**, *196*, 186−193.

(30) Yan, Z.; Lin, J.; Yuan, X.; Song, T.; Yu, C.; Liu, Z.; He, X.; Liang, J.; Tang, C.; Huang, Y. Desulfurization of Model Oil by Selective Adsorption over Porous Boron Nitride Fibers with Tailored Microstructures. *Sci. Rep.* **2017**, *7*, 3297.

(31) Yu, S.; Wang, X.; Pang, H.; Zhang, R.; Song, W.; Fu, D.; Hayat, T.; Wang, X. Boron nitride-based materials for the removal of pollutants from aqueous solutions: A review. *Chem. Eng. J.* **2018**, *333*, 343−360.

(32) Li, S.; Liu, F.; Su, Y.; Shao, N.; Yu, D.; Liu, Y.; Liu, W.; Zhang, Z. Luffa sponge-derived hierarchical meso/macroporous boron nitride fibers as superior sorbents for heavy metal sequestration. *J. Hazard. Mater.* **2019**, *378*, 120669.

(33) Wang, J.; Ai, K.; Lu, L. Flame-retardant porous hexagonal boron nitride for safe and effective radioactive iodine capture. *J. Mater. Chem. A* **2019**, *7*, 16850−16858.

(34) Weng, Q.; Wang, X.; Zhi, C.; Bando, Y.; Golberg, D. Boron Nitride Porous Microbelts for Hydrogen Storage. *ACS Nano* **2013**, *7*, 1558−1565.

(35) Zhang, X.; Lian, G.; Si, H.; Wang, J.; Cui, D.; Wang, Q. Novel BN porous-hollow nanorods: synthesis, tunable dimensions, property and formation mechanism. *J. Mater. Chem. A* **2013**, *1*, 11992−11998.

(36) Kim, J.; Han, J.; Seo, M.; Kang, S.; Kim, D.; Ihm, J. High-surface area ceramic-derived boron-nitride and its hydrogen uptake properties. *J. Mater. Chem. A* **2013**, *1*, 1014−1017.

(37) Weng, Q.; Wang, X.; Bando, Y.; Golberg, D. One-Step Template-Free Synthesis of Highly Porous Boron Nitride Microsponges for Hydrogen Storage. *Adv. Energy Mater.* **2014**, *4*, 1301525.

(38) Lale, A.; Bernard, S.; Demirci, U. B. Boron Nitride for Hydrogen Storage. *ChemPlusChem* **2018**, *83*, 893−903.

(39) Hong, S.; Lee, C.-S.; Lee, M.-H.; Lee, Y.; Ma, K. Y.; Kim, G.; Yoon, S. I.; Ihm, K.; Kim, K.-J.; Shin, T. J.; Kim, S. W.; Jeon, E.-c.; Jeon, H.; Kim, J.-Y.; Lee, H.-I.; Lee, Z.; Antidormi, A.; Roche, S.; Chhowalla, M.; Shin, H.-J.; Shin, H. S. Ultralow-dielectric-constant amorphous boron nitride. *Nature* **2020**, *582*, 511−514.

(40) Golberg, D.; Bando, Y.; Kurashima, K.; Sato, T. Synthesis and Characterization of Ropes made of BN Multiwalled Nanotubes. *Scr. Mater.* **2001**, *44*, 1561−1565.

(41) Chen, Y.; Zou, J.; Campbell, S. J.; Le Caer, G. Boron Nitride Nanotubes: Pronounced Resistance to Oxidation. *Appl. Phys. Lett.* **2004**, *84*, 2430−2432.

(42) Liu, Z.; Gong, Y.; Zhou, W.; Ma, L.; Yu, J.; Idrobo, J. C.; Jung, J.; MacDonald, A. H.; Vajtai, R.; Lou, J.; Ajayan, P. M. Ultrathin High-Temperature Oxidation-Resistant Coatings of Hexagonal Boron Nitride. *Nat. Commun.* **2013**, *4*, 2541.

(43) Li, L. H.; Cervenka, J.; Watanabe, K.; Taniguchi, T.; Chen, Y. Strong Oxidation Resistance of Atomically Thin Boron Nitride Nanosheets. *ACS Nano* **2014**, *8*, 1457−1462.

(44) Grant, J. T.; Carrero, C. A.; Goeltl, F.; Venegas, J.; Mueller, P.; Burt, S. P.; Specht, S. E.; McDermott, W. P.; Chieregato, A.; Hermans, I. Selective Oxidative Dehydrogenation of Propane to Propene using Boron Nitride Catalysts. *Science* **2016**, *354*, 1570.

(45) Shi, L.; Wang, D.; Song, W.; Shao, D.; Zhang, W.-P.; Lu, A.-H. Edge-hydroxylated Boron Nitride for Oxidative Dehydrogenation of Propane to Propylene. *ChemCatChem* **2017**, *9*, 1788−1793.

(46) Huang, R.; Zhang, B.; Wang, J.; Wu, K.-H.; Shi, W.; Zhang, Y.; Liu, Y.; Zheng, A.; Schlögl, R.; Su, D. S. Direct Insight into Ethane Oxidative Dehydrogenation over Boron Nitrides. *ChemCatChem* **2017**, *9*, 3293−3297.

(47) Venegas, J. M.; Grant, J. T.; McDermott, W. P.; Burt, S. P.; Micka, J.; Carrero, C. A.; Hermans, I. Selective Oxidation of*n*-Butane and Isobutane Catalyzed by Boron Nitride. *ChemCatChem* **2017**, *9*, 2118−2127.

(48) Li, P.; Li, H.; Pan, X.; Tie, K.; Cui, T.; Ding, M.; Bao, X. Catalytically Active Boron Nitride in Acetylene Hydrochlorination. *ACS Catal.* **2017**, *7*, 8572−8577.

(49) Blase, X.; Rubio, A.; Louie, S. G.; Cohen, M. L. Quasiparticle band structure of bulk hexagonal boron nitride and related systems. *Phys. Rev. B: Condens. Matter Mater. Phys.* **1995**, *51*, 6868−6875.

(50) Watanabe, K.; Taniguchi, T.; Kanda, H. Direct-bandgap properties and evidence for ultraviolet lasing of hexagonal boron nitride single crystal. *Nat. Mater.* **2004**, *3*, 404−409.

(51) Golberg, D.; Bando, Y.; Huang, Y.; Terao, T.; Mitome, M.; Tang, C.; Zhi, C. Boron Nitride Nanotubes and Nanosheets. *ACS Nano* **2010**, *4*, 2979−2993.

(52) Song, L.; Ci, L.; Lu, H.; Sorokin, P. B.; Jin, C.; Ni, J.; Kvashnin, A. G.; Kvashnin, D. G.; Lou, J.; Yakobson, B. I.; Ajayan, P. M. Large Scale Growth and Characterization of Atomic Hexagonal Boron Nitride Layers. *Nano Lett.* **2010**, *10*, 3209−3215.

(53) Tran, T. T.; Bray, K.; Ford, M. J.; Toth, M.; Aharonovich, I. Quantum emission from hexagonal boron nitride monolayers. *Nat. Nanotechnol.* **2016**, *11*, 37−41.

(54) Tran, T. T.; Elbadawi, C.; Totonjian, D.; Lobo, C. J.; Grosso, G.; Moon, H.; Englund, D. R.; Ford, M. J.; Aharonovich, I.; Toth, M. Robust Multicolor Single Photon Emission from Point Defects in Hexagonal Boron Nitride. *ACS Nano* **2016**, *10*, 7331−7338.

(55) Bourrellier, R.; Meuret, S.; Tararan, A.; Stéphan, O.; Kociak, M.; Tizei, L. H. G.; Zobelli, A. Bright UV Single Photon Emission at Point Defects in h-BN. *Nano Lett.* **2016**, *16*, 4317−4321.

(56) Xu, Z.-Q.; Elbadawi, C.; Tran, T. T.; Kianinia, M.; Li, X.; Liu, D.; Hoffman, T. B.; Nguyen, M.; Kim, S.; Edgar, J. H.; Wu, X.; Song, L.; Ali,

S.; Ford, M.; Toth, M.; Aharonovich, I. Single photon emission from plasma treated 2D hexagonal boron nitride. *Nanoscale* **2018**, *10*, 7957−7965.

(57) Han, W.-Q.; Brutchey, R.; Tilley, T. D.; Zettl, A. Activated Boron Nitride Derived from Activated Carbon. *Nano Lett.* **2004**, *4*, 173−176.

(58) Vinu, A.; Terrones, M.; Golberg, D.; Hishita, S.; Ariga, K.; Mori, T. Synthesis of Mesoporous BN and BCN Exhibiting Large Surface Areas via Templating Methods. *Chem. Mater.* **2005**, *17*, 5887−5890.

(59) Dibandjo, P.; Chassagneux, F.; Bois, L.; Sigala, C.; Miele, P. Comparison between SBA-15 silica and CMK-3 carbon nanocasting for mesoporous boron nitride synthesis. *J. Mater. Chem.* **2005**, *15*, 1917−1923.

(60) Rushton, B.; Mokaya, R. Mesoporous boron nitride and boron-nitride-carbon materials from mesoporous silica templates. *J. Mater. Chem.* **2008**, *18*, 235−241.

(61) Alauzun, J. G.; Ungureanu, S.; Brun, N.; Bernard, S.; Miele, P.; Backov, R.; Sanchez, C. Novel monolith-type boron nitride hierarchical foams obtained through integrative chemistry. *J. Mater. Chem.* **2011**, *21*, 14025−14030.

(62) Schlienger, S.; Alauzun, J.; Michaux, F.; Vidal, L.; Parmentier, J.; Gervais, C.; Babonneau, F.; Bernard, S.; Miele, P.; Parra, J. B. Micro-, Mesoporous Boron Nitride-Based Materials Templated from Zeolites. *Chem. Mater.* **2012**, *24*, 88−96.

(63) Maleki, M.; Beitollahi, A.; Shokouhimehr, M. Simple Synthesis of Two-Dimensional Micro/Mesoporous Boron Nitride. *Eur. J. Inorg. Chem.* **2015**, *2015*, 2478−2485.

(64) Xue, Y.; Dai, P.; Jiang, X.; Wang, X.; Zhang, C.; Tang, D.; Weng, Q.; Wang, X.; Pakdel, A.; Tang, C.; Bando, Y.; Golberg, D. Template-free synthesis of boron nitride foam-like porous monoliths and their high-end applications in water purification. *J. Mater. Chem. A* **2016**, *4*, 1469−1478.

(65) Marchesini, S.; McGilvery, C. M.; Bailey, J.; Petit, C. Template-Free Synthesis of Highly Porous Boron Nitride: Insights into Pore Network Design and Impact on Gas Sorption. *ACS Nano* **2017**, *11*, 10003−10011.

(66) Marchesini, S.; Regoutz, A.; Payne, D.; Petit, C. Tunable porous boron nitride: Investigating its formation and its application for gas adsorption. *Microporous Mesoporous Mater.* **2017**, *243*, 154−163.

(67) Yang, C.; Wang, J.; Chen, Y.; Liu, D.; Huang, S.; Lei, W. One-step template-free synthesis of 3D functionalized flower-like boron nitride nanosheets for NH3 and CO2 adsorption. *Nanoscale* **2018**, *10*, 10979−10985.

(68) Shankar, R.; Marchesini, S.; Petit, C. Enhanced Hydrolytic Stability of Porous Boron Nitride via the Control of Crystallinity, Porosity, and Chemical Composition. *J. Phys. Chem. C* **2019**, *123*, 4282−4290.

(69) Murakami, M.; Shimizu, T.; Tansho, M.; Vinu, A.; Ariga, K.; Takegoshi, K. Chemically Nonequivalent Sites in Mesoporous BCN Revealed by Solid-state NMR at 21.8 T. *Chem. Lett.* **2006**, *35*, 986−987.

(70) Maciel, G. E.; Sindorf, D. W. Silicon-29 NMR study of the surface of silica gel by cross polarization and magic-angle spinning. *J. Am. Chem. Soc.* **1980**, *102*, 7606−7607.

(71) Sindorf, D. W.; Maciel, G. E. Silicon-29 NMR study of dehydrated/rehydrated silica gel using cross polarization and magic-angle spinning. *J. Am. Chem. Soc.* **1983**, *105*, 1487−1493.

(72) Morris, H. D.; Ellis, P. D. Aluminum-27 cross polarization of aluminas. The NMR spectroscopy of surface aluminum atoms. *J. Am. Chem. Soc.* **1989**, *111*, 6045−6049.

(73) Lelli, M.; Gajan, D.; Lesage, A.; Caporini, M. A.; Vitzthum, V.; Miéville, P.; Héroguel, F.; Rascón, F.; Roussey, A.; Thieuleux, C.; Boualleg, M.; Veyre, L.; Bodenhausen, G.; Coperet, C.; Emsley, L. Fast Characterization of Functionalized Silica Materials by Silicon-29 Surface-Enhanced NMR Spectroscopy Using Dynamic Nuclear Polarization. *J. Am. Chem. Soc.* **2011**, *133*, 2104−2107.

(74) Taoufik, M.; Szeto, K. C.; Merle, N.; Rosal, I. D.; Maron, L.; Trébosc, J.; Tricot, G.; Gauvin, R. M.; Delevoye, L. Heteronuclear NMR Spectroscopy as a Surface-Selective Technique: A Unique Look at the Hydroxyl Groups of γ-Alumina. *Chem.—Eur. J.* **2014**, *20*, 4038−4046.

(75) Dorn, R. W.; Ryan, M. J.; Kim, T.-H.; Goh, T. W.; Venkatesh, A.; Heintz, P. M.; Zhou, L.; Huang, W.; Rossini, A. J. Identifying the Molecular Edge Termination of Exfoliated Hexagonal Boron Nitride Nanosheets with Solid-State NMR Spectroscopy and Plane-Wave DFT Calculations. *Chem. Mater.* **2020**, *32*, 3109−3121.

(76) Dorn, R. W.; Cendejas, M. C.; Chen, K.; Hung, I.; Altvater, N. R.; McDermott, W. P.; Gan, Z.; Hermans, I.; Rossini, A. J. Structure Determination of Boron-Based Oxidative Dehydrogenation Heterogeneous Catalysts With Ultrahigh Field 35.2 T 11B Solid-State NMR Spectroscopy. *ACS Catal.* **2020**, *10*, 13852−13866.

(77) Hu, Y.; Shim, Y.; Oh, J.; Park, S.; Park, S.; Ishii, Y. Synthesis of 13C-,15N-Labeled Graphitic Carbon Nitrides and NMR-Based Evidence of Hydrogen-Bonding Assisted Two-Dimensional Assembly. *Chem. Mater.* **2017**, *29*, 5080−5089.

(78) Sakellariou, D.; Lesage, A.; Hodgkinson, P.; Emsley, L. Homonuclear dipolar decoupling in solid-state NMR using continuous phase modulation. *Chem. Phys. Lett.* **2000**, *319*, 253−260.

(79) Gastreich, M.; Marian, C. M. Ab initio prediction of15N-NMR chemical shift in ?-boron nitride based on an analysis of connectivities. *J. Comput. Chem.* **1998**, *19*, 716−725.

(80) Gervais, C.; Babonneau, F. High resolution solid state NMR investigation of various boron nitride preceramic polymers. *J. Organomet. Chem.* **2002**, *657*, 75−82.

(81) Lesage, A.; Lelli, M.; Gajan, D.; Caporini, M. A.; Vitzthum, V.; Miéville, P.; Alauzun, J.; Roussey, A.; Thieuleux, C.; Mehdi, A.; Bodenhausen, G.; Coperet, C.; Emsley, L. Surface Enhanced NMR Spectroscopy by Dynamic Nuclear Polarization. *J. Am. Chem. Soc.* **2010**, *132*, 15459−15461.

(82) Rossini, A. J.; Zagdoun, A.; Lelli, M.; Lesage, A.; Copéret, C.; Emsley, L. Dynamic Nuclear Polarization Surface Enhanced NMR Spectroscopy. *Acc. Chem. Res.* **2013**, *46*, 1942−1951.

(83) Zhao, X.; Sudmeier, J. L.; Bachovchin, W. W.; Levitt, M. H. Measurement of NH Bond Lengths by Fast Magic-Angle Spinning Solid-State NMR Spectroscopy: A New Method for the Quantification of Hydrogen Bonds. *J. Am. Chem. Soc.* **2001**, *123*, 11097−11098.

(84) Zhao, X.; Hoffbauer, W.; Levitt, M. H.; Schmedt auf der Günne, J. Heteronuclear polarization transfer by symmetry-based recoupling sequences in solid-state NMR. *Solid State Nucl. Magn. Reson.* **2004**, *26*, 57−64.

(85) Carnahan, S. L.; Lampkin, B. J.; Naik, P.; Hanrahan, M. P.; Slowing, I. I.; VanVeller, B.; Wu, G.; Rossini, A. J. Probing O-H Bonding through Proton Detected 1H-17O Double Resonance Solid-State NMR Spectroscopy. *J. Am. Chem. Soc.* **2019**, *141*, 441−450.

(86) Duong, N. T.; Rossi, F.; Makrinich, M.; Goldbourt, A.; Chierotti, M. R.; Gobetto, R.; Nishiyama, Y. Accurate 1H-14N distance measurements by phase-modulated RESPDOR at ultra-fast MAS. *J. Magn. Reson.* **2019**, *308*, 106559.

(87) Hong, M.; Gross, J. D.; Rienstra, C. M.; Griffin, R. G.; Kumashiro, K. K.; Schmidt-Rohr, K. Coupling Amplification in 2D MAS NMR and Its Application to Torsion Angle Determination in Peptides. *J. Magn. Reson.* **1997**, *129*, 85−92.

(88) Gervais, C.; Framery, E.; Duriez, C.; Maquet, J.; Vaultier, M.; Babonneau, F. 11B and 15N solid state NMR investigation of a boron nitride preceramic polymer prepared by ammonolysis of borazine. *J. Eur. Ceram. Soc.* **2005**, *25*, 129−135.

(89) Jeschke, G.; Jansen, M. High-Resolution14N Solid-State NMR Spectroscopy. *Angew. Chem., Int. Ed.* **1998**, *37*, 1282−1283.

(90) Cavadini, S.; Antonijevic, S.; Lupulescu, A.; Bodenhausen, G. Indirect detection of nitrogen-14 in solids via protons by nuclear magnetic resonance spectroscopy. *J. Magn. Reson.* **2006**, *182*, 168−172.

(91) Gan, Z.; Amoureux, J. P.; Trébosc, J. Proton-detected 14N MAS NMR using homonuclear decoupled rotary resonance. *Chem. Phys. Lett.* **2007**, *435*, 163−169.

(92) Cavadini, S. Indirect detection of nitrogen-14 in solid-state NMR spectroscopy. *Prog. Nucl. Magn. Reson. Spectrosc.* **2010**, *56*, 46−77.

(93) Nishiyama, Y.; Endo, Y.; Nemoto, T.; Utsumi, H.; Yamauchi, K.; Hioka, K.; Asakura, T. Very fast magic angle spinning 1H-14N 2D solid-state NMR: Sub-micro-liter sample data collection in a few minutes. *J. Magn. Reson.* **2011**, *208*, 44−48.

(94) Tatton, A. S.; Jonathan, P. B.; Dinu, I.; Steven, P. B. 14N−1H Heteronuclear Multiple-Quantum Correlation Magic-Angle Spinning NMR Spectroscopy of Organic Solids. *Z. Phys. Chem.* **2012**, *226*, 1187−1204.

(95) Tatton, A. S.; Pham, T. N.; Vogt, F. G.; Iuga, D.; Edwards, A. J.; Brown, S. P. Probing Hydrogen Bonding in Cocrystals and Amorphous Dispersions Using 14N-1H HMQC Solid-State NMR. *Mol. Pharmaceutics* **2013**, *10*, 999−1007.

(96) Wijesekara, A. V.; Venkatesh, A.; Lampkin, B. J.; VanVeller, B.; Lubach, J. W.; Nagapudi, K.; Hung, I.; Gor'kov, P. L.; Gan, Z.; Rossini, A. J. Fast Acquisition of Proton-Detected HETCOR Solid-State NMR Spectra of Quadrupolar Nuclei and Rapid Measurement of NH Bond Lengths by Frequency Selective HMQC and RESPDOR Pulse Sequences. *Chem.—Eur. J.* **2020**, *26*, 7881−7888.

(97) Gan, Z. Measuring Amide Nitrogen Quadrupolar Coupling by High-Resolution 14N/13C NMR Correlation under Magic-Angle Spinning. *J. Am. Chem. Soc.* **2006**, *128*, 6040−6041.

(98) Jeschke, G.; Hoffbauer, W.; Jansen, M. A comprehensive NMR study of cubic and hexagonal boron nitride. *Solid State Nucl. Magn. Reson.* **1998**, *12*, 1−7.

(99) Kentgens, A. P. M. A Practical Guide to Solid-State NMR of Half-Integer Quadrupolar Nuclei with some Applications to Disordered Systems. *Geoderma* **1997**, *80*, 271−306.

(100) Ashbrook, S. E.; Duer, M. J. Structural Information from Quadrupolar Nuclei in Solid State NMR. *Concepts Magn. Reson., Part A* **2006**, *28A*, 183−248.

(101) Angel Wong, Y.-T.; Bryce, D. L. Recent Advances in 11B Solid-State Nuclear Magnetic Resonance Spectroscopy of Crystalline Solids. *Annual Reports on NMR Spectroscopy*; Webb, G. A., Ed.; Academic Press, 2018; Vol. *93*, pp 213−279.

(102) Gan, Z.; Hung, I.; Wang, X.; Paulino, J.; Wu, G.; Litvak, I. M.; Gor'kov, P. L.; Brey, W. W.; Lendi, P.; Schiano, J. L.; Bird, M. D.; Dixon, I. R.; Toth, J.; Boebinger, G. S.; Cross, T. A. NMR Spectroscopy up to 35.2T using a Series-Connected Hybrid Magnet. *J. Magn. Reson.* **2017**, *284*, 125−136.

(103) Keeler, E. G.; Michaelis, V. K.; Colvin, M. T.; Hung, I.; Gor'kov, P. L.; Cross, T. A.; Gan, Z.; Griffin, R. G. 17O MAS NMR Correlation Spectroscopy at High Magnetic Fields. *J. Am. Chem. Soc.* **2017**, *139*, 17953−17963.

(104) Bonhomme, C.; Wang, X.; Hung, I.; Gan, Z.; Gervais, C.; Sassoye, C.; Rimsza, J.; Du, J.; Smith, M. E.; Hanna, J. V.; Sarda, S.; Gras, P.; Combes, C.; Laurencin, D. Pushing the Limits of Sensitivity and Resolution for Natural Abundance 43Ca NMR using Ultra-High Magnetic Field (35.2 T). *Chem. Commun.* **2018**, *54*, 9591−9594.

(105) Shen, J.; Terskikh, V.; Wang, X.; Hung, I.; Gan, Z.; Wu, G. A Quadrupole-Central-Transition 17O NMR Study of Nicotinamide: Experimental Evidence of Cross-Correlation between Second-Order Quadrupolar Interaction and Magnetic Shielding Anisotropy. *J. Phys. Chem. B* **2018**, *122*, 4813−4820.

(106) Keeler, E. G.; Michaelis, V. K.; Wilson, C. B.; Hung, I.; Wang, X.; Gan, Z.; Griffin, R. G. High-Resolution 17O NMR Spectroscopy of Structural Water. *J. Phys. Chem. B* **2019**, *123*, 3061−3067.

(107) Madsen, R. S. K.; Qiao, A.; Sen, J.; Hung, I.; Chen, K.; Gan, Z.; Sen, S.; Yue, Y. Ultrahigh-field 67 Zn NMR reveals short-range disorder in zeolitic imidazolate framework glasses. *Science* **2020**, *367*, 1473.

(108) Shen, L.; Wang, Y.; Du, J. H.; Chen, K.; Lin, Z.; Wen, Y.; Hung, I.; Gan, Z.; Peng, L. Probing Interactions of γ-Alumina with Water via Multinuclear Solid-State NMR Spectroscopy. *ChemCatChem* **2020**, *12*, 1569−1574.

(109) Chen, K.; Horstmeier, S.; Nguyen, V. T.; Wang, B.; Crossley, S. P.; Pham, T.; Gan, Z.; Hung, I.; White, J. L. Structure and Catalytic Characterization of a Second Framework Al(IV) Site in Zeolite Catalysts Revealed by NMR at 35.2 T. *J. Am. Chem. Soc.* **2020**, *142*, 7514−7523.

(110) Wang, Q.; Li, W.; Hung, I.; Mentink-Vigier, F.; Wang, X.; Qi, G.; Wang, X.; Gan, Z.; Xu, J.; Deng, F. Mapping the oxygen structure of γ-Al2O3 by high-field solid-state NMR spectroscopy. *Nat. Commun.* **2020**, *11*, 3620.

(111) Martins, V.; Xu, J.; Wang, X.; Chen, K.; Hung, I.; Gan, Z.; Gervais, C.; Bonhomme, C.; Jiang, S.; Zheng, A.; Lucier, B. E. G.; Huang, Y. Higher Magnetic Fields, Finer MOF Structural Information: 17O Solid-State NMR at 35.2 T. *J. Am. Chem. Soc.* **2020**, *142*, 14877−14889.

(112) Love, A. M.; Thomas, B.; Specht, S. E.; Hanrahan, M. P.; Venegas, J. M.; Burt, S. P.; Grant, J. T.; Cendejas, M. C.; McDermott, W. P.; Rossini, A. J.; Hermans, I. Probing the Transformation of Boron Nitride Catalysts under Oxidative Dehydrogenation Conditions. *J. Am. Chem. Soc.* **2019**, *141*, 182−190.

(113) Kroeker, S.; Stebbins, J. F. Three-Coordinated Boron-11 Chemical Shifts in Borates. *Inorg. Chem.* **2001**, *40*, 6239−6246.

(114) Murakami, M.; Shimizu, T.; Tansho, M.; Vinu, A.; Ariga, K.; Mori, T.; Takegoshi, K. Two-dimensional 11B-11B exchange NMR study in mesoporous boron carbon nitride at 21.8T. *Solid State Nucl. Magn. Reson.* **2007**, *31*, 193−196.

(115) Mali, G.; Fink, G.; Taulelle, F. Double-Quantum Homonuclear Correlation Magic Angle Sample Spinning Nuclear Magnetic Resonance Spectroscopy of Dipolar-Coupled Quadrupolar Nuclei. *J. Chem. Phys.* **2004**, *120*, 2835−2845.

(116) Edén, M.; Zhou, D.; Yu, J. Improved Double-Quantum NMR Correlation Spectroscopy of Dipolar-Coupled Quadrupolar Spins. *Chem. Phys. Lett.* **2006**, *431*, 397−403.

(117) Wang, Q.; Hu, B.; Lafon, O.; Trébosc, J.; Deng, F.; Amoureux, J. P. Double-Quantum Homonuclear NMR Correlation Spectroscopy of Quadrupolar Nuclei Subjected to Magic-Angle Spinning and High Magnetic Field. *J. Magn. Reson.* **2009**, *200*, 251−260.

(118) Feng, N.; Wang, Q.; Zheng, A.; Zhang, Z.; Fan, J.; Liu, S.-B.; Amoureux, J.-P.; Deng, F. Understanding the High Photocatalytic Activity of (B, Ag)-Codoped TiO2 under Solar-Light Irradiation with XPS, Solid-State NMR, and DFT Calculations. *J. Am. Chem. Soc.* **2013**, *135*, 1607−1616.

(119) Yu, Y.; Stevensson, B.; Edén, M. Medium-Range Structural Organization of Phosphorus-Bearing Borosilicate Glasses Revealed by Advanced Solid-State NMR Experiments and MD Simulations: Consequences of B/Si Substitutions. *J. Phys. Chem. B* **2017**, *121*, 9737−9752.

(120) Brus, J.; Czernek, J.; Urbanova, M.; Kobera, L.; Jegorov, A. An efficient 2D 11B-11B solid-state NMR spectroscopy strategy for monitoring covalent self-assembly of boronic acid-derived compounds: the transformation and unique architecture of bortezomib molecules in the solid state. *Phys. Chem. Chem. Phys.* **2017**, *19*, 487−495.

(121) Yu, Y.; Stevensson, B.; Edén, M. Direct Experimental Evidence for Abundant BO4-BO4 Motifs in Borosilicate Glasses From Double-Quantum 11B NMR Spectroscopy. *J. Phys. Chem. Lett.* **2018**, *9*, 6372−6376.

(122) Märker, K.; Hediger, S.; De Paëpe, G. Efficient 2D Double-Quantum Solid-State NMR Spectroscopy with Large Spectral Widths. *Chem. Commun.* **2017**, *53*, 9155−9158.

(123) Gan, Z. Measuring multiple carbon-nitrogen distances in natural abundant solids using R-RESPDOR NMR. *Chem. Commun.* **2006**, *45*, 4712−4714.

(124) Charpentier, T. The PAW/GIPAW approach for computing NMR parameters: A new dimension added to NMR study of solids. *Solid State Nucl. Magn. Reson.* **2011**, *40*, 1−20.

(125) Bonhomme, C.; Gervais, C.; Babonneau, F.; Coelho, C.; Pourpoint, F.; Azaïs, T.; Ashbrook, S. E.; Griffin, J. M.; Yates, J. R.; Mauri, F.; Pickard, C. J. First-Principles Calculation of NMR Parameters Using the Gauge Including Projector Augmented Wave Method: A Chemist's Point of View. *Chem. Rev.* **2012**, *112*, 5733−5779.

(126) Ferrara, C.; Tealdi, C.; Pedone, A.; Menziani, M. C.; Rossini, A. J.; Pintacuda, G.; Mustarelli, P. Local versus Average Structure in LaSrAl3O7: A NMR and DFT Investigation. *J. Phys. Chem. C* **2013**, *117*, 23451−23458.

(127) Njegic, B.; Levin, E. M.; Schmidt-Rohr, K. 125Te NMR chemical-shift trends in PbTe-GeTe and PbTe-SnTe alloys. *Solid State Nucl. Magn. Reson.* **2013**, *55−56*, 79−83.

(128) de Souza, F. A. L.; Ambrozio, A. R.; Souza, E. S.; Cipriano, D. F.; Scopel, W. L.; Freitas, J. C. C. NMR Spectral Parameters in Graphene,

Graphite, and Related Materials: Ab Initio Calculations and Experimental Results. *J. Phys. Chem. C* **2016**, *120*, 27707−27716.

(129) Ryan, B. J.; Hanrahan, M. P.; Wang, Y.; Ramesh, U.; Nyamekye, C. K. A.; Nelson, R. D.; Liu, Z.; Huang, C.; Whitehead, B.; Wang, J.; Roling, L. T.; Smith, E. A.; Rossini, A. J.; Panthani, M. G. Silicene, Siloxene, or Silicane? Revealing the Structure and Optical Properties of Silicon Nanosheets Derived from Calcium Disilicide. *Chem. Mater.* **2020**, *32*, 795−804.

(130) Mark, L. O.; Dorn, R. W.; McDermott, W. P.; Agbi, T. O.; Altvater, N. R.; Jansen, J.; Lebrón-Rodríguez, E. A.; Cendejas, M. C.; Rossini, A. J.; Hermans, I. Highly Selective Carbon-Supported Boron for Oxidative Dehydrogenation of Propane. *ChemCatChem* **2021**, *13*, 3611−3618.

(131) Pickard, C. J.; Mauri, F. All-electron magnetic response with pseudopotentials: NMR chemical shifts. *Phys. Rev. B: Condens. Matter Mater. Phys.* **2001**, *63*, 245101.

(132) Clark, S. J.; Segall, M. D.; Pickard, C. J.; Hasnip, P. J.; Probert, M. I. J.; Refson, K.; Payne, M. C. First principles methods using CASTEP. *Z. Kristallogr.-Cryst. Mater.* **2005**, *220*, 567−570.

(133) Perdew, J. P.; Burke, K.; Ernzerhof, M. Generalized Gradient Approximation Made Simple. *Phys. Rev. Lett.* **1996**, *77*, 3865−3868.

(134) Tkatchenko, A.; Scheffler, M. Accurate Molecular Van Der Waals Interactions from Ground-State Electron Density and Free-Atom Reference Data. *Phys. Rev. Lett.* **2009**, *102*, 073005.

(135) Vanderbilt, D. Soft self-consistent pseudopotentials in a generalized eigenvalue formalism. *Phys. Rev. B: Condens. Matter Mater. Phys.* **1990**, *41*, 7892−7895.

(136) Yates, J. R.; Pickard, C. J.; Mauri, F. Calculation of NMR chemical shifts for extended systems using ultrasoft pseudopotentials. *Phys. Rev. B: Condens. Matter Mater. Phys.* **2007**, *76*, 024401.

(137) Green, T. F. G.; Yates, J. R. Relativistic nuclear magnetic resonance J-coupling with ultrasoft pseudopotentials and the zeroth-order regular approximation. *J. Chem. Phys.* **2014**, *140*, 234106.

(138) Pease, R. S. Crystal Structure of Boron Nitride. *Nature* **1950**, *165*, 722−723.

(139) Bak, M.; Rasmussen, J. T.; Nielsen, N. C. SIMPSON: A General Simulation Program for Solid-State NMR Spectroscopy. *J. Magn. Reson.* **2000**, *147*, 296−330.

(140) Tošner, Z.; Vosegaard, T.; Kehlet, C.; Khaneja, N.; Glaser, S. J.; Nielsen, N. C. Optimal control in NMR spectroscopy: Numerical implementation in SIMPSON. *J. Magn. Reson.* **2009**, *197*, 120−134.

(141) Tošner, Z.; Andersen, R.; Stevensson, B.; Edén, M.; Nielsen, N. C.; Vosegaard, T. Computer-intensive simulation of solid-state NMR experiments using SIMPSON. *J. Magn. Reson.* **2014**, *246*, 79−93.

(142) van Meerten, S. G. J.; Franssen, W. M. J.; Kentgens, A. P. M. ssNake: A Cross-Platform Open-Source NMR Data Processing and Fitting Application. *J. Magn. Reson.* **2019**, *301*, 56−66.

(143) Harris, R. K.; Becker, E. D.; Cabral de Menezes, S. M.; Goodfellow, R.; Granger, P. NMR Nomenclature: Nuclear Spin Properties and Conventions for Chemical Shifts: IUPAC Recommendations 2001. *Solid State Nucl. Magn. Reson.* **2002**, *22*, 458−483.

(144) Brinkmann, A.; Kentgens, A. P. M. Proton-Selective 17O−H Distance Measurements in Fast Magic-Angle-Spinning Solid-State NMR Spectroscopy for the Determination of Hydrogen Bond Lengths. *J. Am. Chem. Soc.* **2006**, *128*, 14758−14759.

(145) Brown, S. P.; Wimperis, S. Two-Dimensional Multiple-Quantum MAS NMR of Quadrupolar Nuclei. Acquisition of the Whole Echo. *J. Magn. Reson.* **1997**, *124*, 279−285.

(146) Hwang, S.-J.; Fernandez, C.; Amoureux, J. P.; Cho, J.; Martin, S. W.; Pruski, M. Quantitative Study of the Short Range Order in B2O3 and B2S3 by MAS and Two-Dimensional Triple-Quantum MAS 11B NMR. *Solid State Nucl. Magn. Reson.* **1997**, *8*, 109−121.

(147) Medek, A.; Harwood, J. S.; Frydman, L. Multiple-Quantum Magic-Angle Spinning NMR: A New Method for the Study of Quadrupolar Nuclei in Solids. *J. Am. Chem. Soc.* **1995**, *117*, 12779−12787.

(148) Fung, B. M.; Khitrin, A. K.; Ermolaev, K. An Improved Broadband Decoupling Sequence for Liquid Crystals and Solids. *J. Magn. Reson.* **2000**, *142*, 97−101.

(149) Yao, Z.; Kwak, H.-T.; Sakellariou, D.; Emsley, L.; Grandinetti, P. J. Sensitivity Enhancement of the Central Transition NMR Signal of Quadrupolar Nuclei under Magic-Angle Spinning. *Chem. Phys. Lett.* **2000**, *327*, 85−90.

(150) Kwak, H.-T.; Prasad, S.; Clark, T.; Grandinetti, P. J. Enhancing Sensitivity of Quadrupolar Nuclei in Solid-State NMR with Multiple Rotor Assisted Population Transfers. *Solid State Nucl. Magn. Reson.* **2003**, *24*, 71−77.

(151) Lee, M.; Goldburg, W. I. Nuclear-Magnetic-Resonance Line Narrowing by a Rotating rf Field. *Phys. Rev.* **1965**, *140*, A1261−A1271.

(152) Bielecki, A.; Kolbert, A. C.; Levitt, M. H. Frequency-switched pulse sequences: Homonuclear decoupling and dilute spin NMR in solids. *Chem. Phys. Lett.* **1989**, *155*, 341−346.

▣ Recommended by ACS